Ore Geology Reviews 72 (2016) 746–759

Contents lists available at ScienceDirect

Ore Geology Reviews

journal homepage: www.elsevier.com/locate/oregeorev

In-situ LA–ICP–MS trace elements analysis of magnetite: The Fenghuangshan Cu–Fe–Au deposit, Tongling, Eastern China

Xiao-Wen Huang [a], Jian-Feng Gao [a,*], Liang Qi [a,b], Yu-Miao Meng [a], Yi-Chang Wang [a,c], Zhi-Hui Dai [a]

[a] State Key Laboratory of Ore Deposit Geochemistry, Institute of Geochemistry, Chinese Academy of Sciences, Guiyang 550081, China
[b] State Key Laboratory of Continental Dynamics, Department of Geology, Northwest University, Xi'an 710069, China
[c] University of Chinese Academy of Sciences, Beijing 100049, China

ARTICLE INFO

Article history:
Received 30 June 2015
Received in revised form 9 September 2015
Accepted 14 September 2015
Available online 25 September 2015

Keywords:
Trace element
LA–ICP–MS
Magnetite
Skarn
Fenghuangshan
Eastern China

ABSTRACT

The Fenghuangshan deposit is a typical Cu–Fe–Au skarn deposit in the Tongling area, Anhui province, Eastern China. The deposit has a paragenetic sequence of a prograde skarn stage, followed by a retrograde skarn stage, and a final quartz–sulfide and carbonate stages. Magnetite in the Fenghuangshan deposit mainly formed in the retrograde and carbonate stages. According to the morphology of magnetite and mineral assemblage of ores, we divided magnetite-bearing ores into three groups. Group 1 (early retrograde skarn stage) is represented by a mineral assemblage of magnetite and chalcopyrite. Group 2 (late retrograde skarn stage) has a mineral assemblage of magnetite, chalcopyrite, and wollastonite with characteristic ring-like magnetite. Group 3 (carbonate stage) is characterized by large amounts of calcite veins crosscut or associated with magnetite and intensive hematization of magnetite crosscut by the veins.

Laser ablation (LA)–ICP–MS was used to determine trace element concentrations of magnetite from the three mineralization stages. Positive correlations among Mg, Al, Ca, and Si in magnetite indicate that these lithophile elements have similar behavior during the skarn formation process. Calcium is an important discriminant element for magnetite in skarn deposits. Positive correlations are also evident for Pb, Sn and W in magnetite, which also indicates their similar behavior. In general, magnetite grains of different stages have similar normalized trace element patterns, indicating that they share a common source. However, some elements such as Co and Mn in magnetite decrease from early retrograde skarn stage, late retrograde skarn stage to carbonate stage, which may be attributed to the precipitation of coexisting minerals (sulfides and carbonates) or the decreasing temperature. Magnetite grains of the retrograde stage have higher Mg + Mn and Si + Al contents than those of the carbonate stage, indicating a decreasing degree of fluid–rock interaction during the skarn formation process. Trace element data of skarn magnetite indicate a more widely compositional variation than previously suggested. Magnetite from the Fenghuangshan Cu–Fe–Au deposit has similar composition to those from other Cu, Cu–Fe or Cu polymetallic skarn deposits, but different from those from Fe skarn deposits, such that magnetite composition is very powerful in establishing the origin of skarn deposits.

1. Introduction

The Fenghuangshan Cu–Fe–Au deposit in Tongling, Anhui province, China, is one of the most important deposits within the Middle-Lower Yangtze River Metallogenic Belt (Fig. 1). The deposit is a skarn-porphyry related to the Late Yanshanian magmatic intrusions emplaced in Lower Triassic limestones (Lai et al., 2007; Shao et al., 2007). The Fe–Cu skarn orebodies (141.1 ± 1.4 Ma, molybdenite Re–Os age; (Qu et al., 2012) were formed by replacement of Lower Triassic limestones by fluids associated with granodiorite and granodiorite porphyry intrusions. The later porphyry Cu mineralization is related to a quartz monzodiorite porphyry stock which crosscuts the previous skarn. Numerous studies of this deposit have focused on the age and geochemistry of intrusions (Li et al., 2014; Qu, 2010; Qu et al., 2012; Qu et al., 2010a), the timing of the mineralization (Li et al., 2014; Qu et al., 2012, Qu et al., 2010c), and the fluid evolution (Lai & Chi, 2007; Lai et al., 2007; Qu et al., 2011, Qu et al., 2010b), but details of Fe skarn mineralization and the compositional variations of magnetite are not well known. As a typical Cu–Fe skarn deposit, the Fenghuangshan deposit provides a good example for revealing the element behavior in magnetite during the skarn formation processes.

Magnetite is a common mineral in igneous, metamorphic, and sedimentary rocks and in many types of mineral deposits (Dupuis & Beaudoin, 2011). Magnetite can form in a variety of physico-chemical environments and contains numerous trace elements, such as Al, Ti, Mg, Mn, Zn, Cr, V, Ni, Co and Ga. The chemical composition of magnetite thus can be used to fingerprint different types of mineral deposits or to

* Corresponding author.
E-mail address: gao_jianfeng@yahoo.com (J.-F. Gao).

http://dx.doi.org/10.1016/j.oregeorev.2015.09.012
0169-1368/

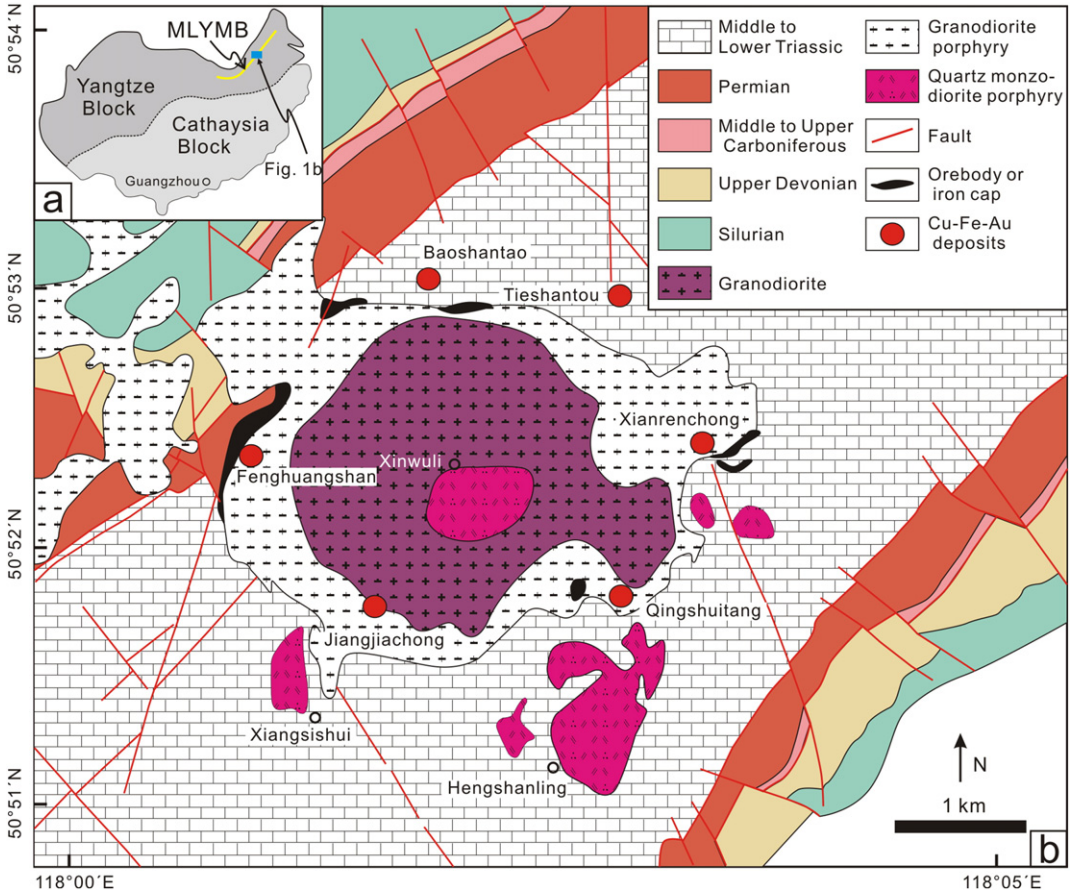

Fig. 1. (a) Simplified geological map showing the location of the Middle-Lower Yangtze River Metallogenic Belt (MLYMB) in the Yangtze Block; (b) Geological map of the Fenghuangshan ore field showing the Xinwuli granitoid intrusions and associated Cu–Fe–Au deposits (modified from Lai et al., 2007).

distinguish different ore forming processes (e.g., Beaudoin & Dupuis, 2009; Carew, 2004; Dare et al., 2015; Dare et al., 2012; Dupuis & Beaudoin, 2011; Hu et al., 2014; Huang et al., 2015; Huang et al., 2013; Huang et al., 2014; Liu et al., 2015; Müller et al., 2003; Nadoll et al., 2014; Nadoll et al., 2012; Nadoll et al., 2015; Rusk et al., 2009; Singoyi et al., 2006). For a specific skarn deposit, trace element concentrations in magnetite can provide important constraints on the fluid evolution of different paragenetic stages and their controlling factors (Hu et al., 2014; Nadoll et al., 2015; Zhao & Zhou, 2015).

In this paper, we describe the ore petrography with emphasis on the magnetite-bearing ores from different mineralization stages of the Fenghuangshan deposit. Trace element compositions of magnetite from ore zones were determined by in situ laser ablation inductively coupled plasma mass spectrometry (LA–ICP–MS). The new dataset provides a better understanding of trace element behavior in magnetite during the skarn formation process. By comparing the compositions of magnetite from the Fenghuangshan deposit with other types of skarn deposits worldwide, we suggest that magnetite from different types of skarn deposits may have different compositions and in turn, the compositional variations can be used to discriminate different origins of skarn magnetite (e.g., Nadoll et al., 2014).

2. Geological background

The Fenghuangshan Cu–Fe–Au deposit is located in the middle of the Middle-Lower Yangtze River Metallogenic Belt along the northern margin of the Yangtze Block in Eastern China (Fig. 1a). The metallogenic belt was controlled by a regional, deep-seated fracture zone called the Yangtze fracture zone, which extends for approximately 450 km from Daye of the Hubei province to Zhenjiang of the Jiangsu province (Chang et al., 1991). This fracture zone was considered to have formed in the Neoproterozoic and re-activated during the Late Jurassic to Late Cretaceous due to the collision between the Yangtze Block and the North China Block (Mao et al., 2011; Pan & Dong, 1999; Zhai et al., 1992; Zhao et al., 1999). Extensive, contemporary intermediate to felsic magmatism along the fracture zone resulted in the emplacement of volcanic and intrusive rocks, and related porphyry–skarn Cu–Au–Mo–Fe deposits.

The Fenghuangshan deposit is associated with a northeast-trending synclinorium intruded by a granitoid stock (the Xinwuli stock) (Fig. 1b). The Xinwuli stock, composed of granodiorite in the center and granodiorite porphyry at the margin, has ages ranging from 119 to 144 Ma (Wu et al., 2000; Zhang et al., 2006). The country rocks consist of Triassic–Permian limestone and dolomitic limestone, which have been transformed into marble forming a 400- to 1200-m-wide thermal metamorphic aureole around the intrusion (Liu & Peng, 2003). A number of Cu–Fe–Au deposits occur near the contact zone between the Xinwuli stock and the country rocks, including the Fenghuangshan, Jiangjiachong, Qingshuitang, Xianrenchong, Tieshantou, and Baoshantao deposits (Fig. 1b). The Fenghuangshan deposit, the largest deposit in the Tongling area, contains 1.38 Mt Fe with an average ore grade of 30.5%, 54,888 t Cu with an average ore grade of 1.24% (Pan & Dong, 1999), and 18.4 t Au with an average ore grade of 0.68 g/t (Chen et al., 2007).

The Fenghuangshan deposit was first discovered as a skarn-type deposit in the contact zone between the granodiorite porphyry and Lower Triassic limestones (Fig. 2). The skarn mineralization was locally overprinted by porphyry-type mineralization related to quartz

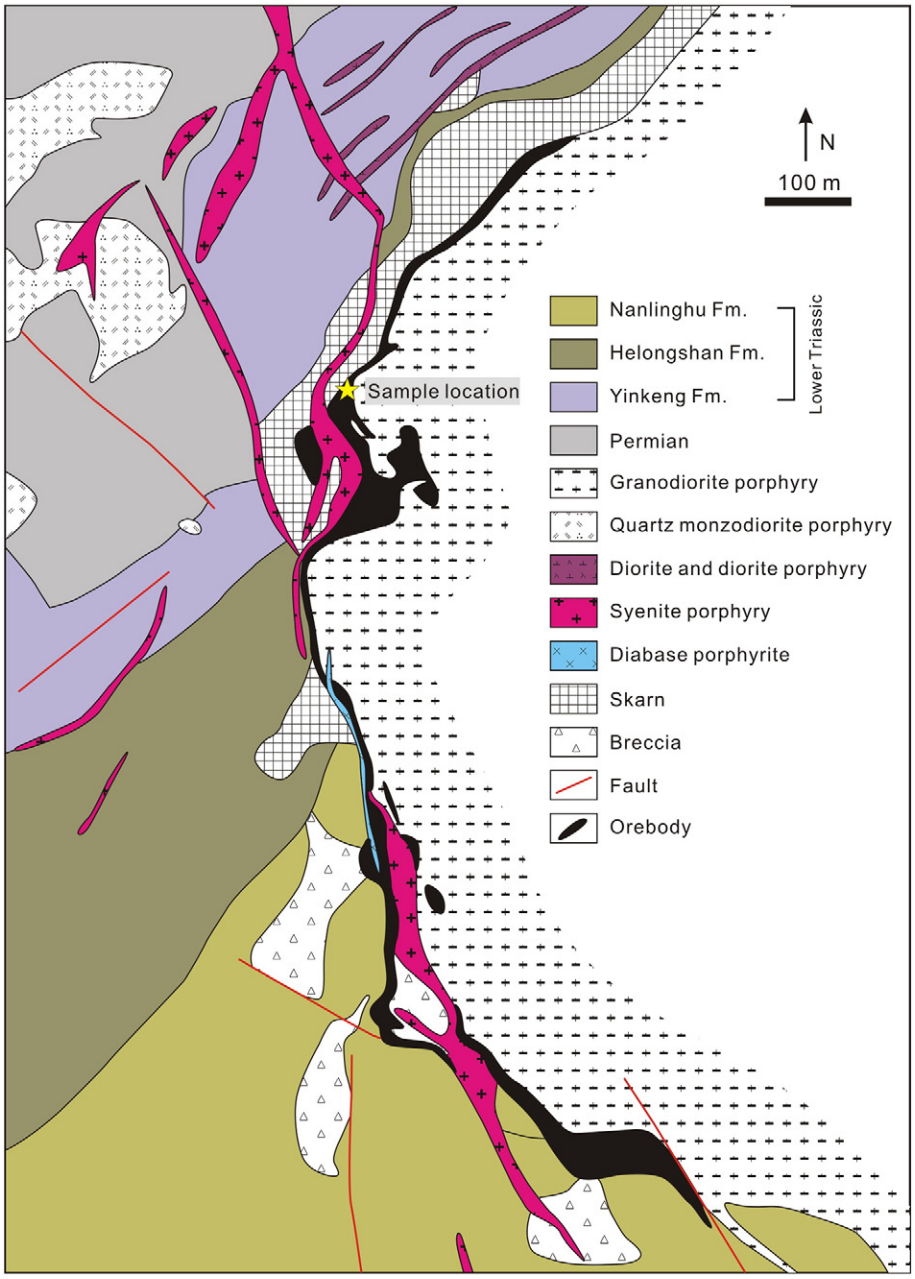

Fig. 2. Plan view geological map of the Fenghuangshan deposit showing the skarn-type mineralization along the contact zone between the granodiorite porphyry and Lower Triassic carbonate rocks (modified from Liu & Peng, 2003).

monzodiorite porphyry stocks (139.4 ± 1.2 Ma, zircon U–Pb age) (Lai & Chi, 2007; Qu et al., 2012; Shao et al., 2007). Copper mineralization occurs in both skarn-type and porphyry-type orebodies, whereas iron mineralization only occurs in the skarn-type orebodies. Most of the skarn was formed by replacement of carbonate rocks (exoskarn), but some occurred within the porphyry rocks (endoskarn). The skarn mineralization occurs in the prograde skarn stage (I), the retrograde skarn stage (II), the quartz–sulfide stage (III), and the carbonate stage (IV) (Qu et al., 2012). Fluid inclusions of diopside, garnet, quartz and calcite have indicated that homogenization temperatures are 478–>600 °C, 448–506 °C, 222–325 °C, and 122–145 °C for the stages I, II, III, and IV, respectively (Lai et al., 2007). Most magnetite was formed in stage II while remaining magnetite is found in stage IV. Ore minerals in the Fenghuangshan skarn are chalcopyrite, pyrite, magnetite, and minor siderite, bornite, sphalerite and galena. Gangue minerals include garnet, diopside, actinolite, tremolite, wollastonite, chlorite, quartz, calcite and epidote.

3. Ore petrography

Samples of iron ores were collected from the mining adit at the middle part —(440 m level) of the Fenghuangshan deposit. According to the ore types and mineral assemblages, these were divided into three groups, corresponding to mineralization stages II and IV. Samples FHS1320 and FHS1321 belong to Group 1, which consist of disseminated magnetite and pyrite. Samples FHS1306, FHS1308, FHS1310, FHS1318, and FHS1319 belong to the second group, represented by massive ore composed of magnetite ± chalcopyrite. Samples FHS1313 and FHS1315 are in the third group, which is composed of massive ore containing great amounts of calcite veins and hematite. Groups 1 and 2 correspond to the early and late retrograde skarn stages, respectively, whereas Group 3 corresponds to the carbonate stage. The detailed ore textures, mineral assemblages and occurrences of magnetite are described as follows.

Ores of Group 1 show clear contact boundaries between mineralized skarn and barren skarn (Fig. 3a). Ores formed at this stage are composed of ~55 vol.% quartz + chlorite, 35 vol.% magnetite, and 10 vol.% chalcopyrite (Figs. 4a and 5a). Magnetite grains have the sizes ranging from ~50 to 250 μm and are commonly replaced by hematite at the margins (Fig. 4a).

Ores of Group 2 are also mainly composed of magnetite and chalcopyrite (Fig. 3b and c), with minor wollastonite, quartz and calcite (Fig. 5b and c). Magnetite occurs as square and hexagonal shapes associated with chalcopyrite, and contains great amounts of approximatively parallel fractures (Fig. 4b). These euhedral magnetite grains range in size from ~100 to 300 μm (Fig. 5c). Magnetite also shows anhedral crystals with a broad spectrum of sizes from ~5 to 50 μm, which is locally replaced by hematite or associated with chalcopyrite (Fig. 4c and d). In part of the ores, the fractures in magnetite are filled by chalcopyrite or calcite, forming zone-like magnetite (Fig. 5d and e).

Magnetite of Group 3 is commonly crosscut by or associated with calcite and chalcopyrite veins (Fig. 3d). Magnetite occurs as fine-grained crystals and is largely replaced by hematite (Fig. 4e and f). Quartz and calcite are the main gangue minerals of the ores at this stage (Fig. 5f).

According to the replacement characteristics of magnetite, large amounts of hydrothermal minerals and absence of exsolution lamellae of ilmenite and spinel in magnetite, are indicative that magnetite in this study is hydrothermal in origin.

4. Analytical methods

Collected ore samples were washed by water and weathered surfaces were removed by cutter. Polished thin sections were prepared from the fresh ore samples and then examined using optical microscopy and scanning electron microscopy (SEM) to characterize the mineralogical and textural relationships, in particular the occurrence, morphology, and texture of magnetite. BSE images of ores are acquired by a Hitachi S-3400 SEM at the Department of Earth Sciences, The University of Hong Kong. Unknown minerals were semi-quantitatively analyzed by energy-dispersive X-ray spectrometry with 1 μm beam diameter at an accelerating voltage of 20 kV. Magnetite grains with grain sizes larger than 44 μm are selected for LA–ICP–MS analysis. Magnetite containing great amounts of silicate and carbonate inclusions or wholly replaced by hematite was not used for LA analysis to avoid signal contamination of other minerals and the effect of later alteration.

Magnetite grains from the different stages of Fe ore formation were analyzed for trace elements at the State Key Laboratory of Ore Deposit Geochemistry, Institute of Geochemistry, Chinese Academy of Sciences, using a Coherent GeoLasPro 193 nm Laser Ablation system coupled with an Agilent 7700x ICP–MS. Analytical methods are available in Gao et al. (Gao et al., 2013) and Huang et al. (Huang et al., 2013). Each analysis includes a ~20 s background acquisition followed by 40 s data acquisition from the sample. Analytical spots (44 μm) were ablated by 160 successive laser pulses (4 Hz). Element contents were calibrated against multiple reference materials, USGS synthetic basalt glass GSE-1G, USGS basalt glass of BCR-2G, BIR-1G and BHVO-2G (http://crustal.usgs.gov/geochemical_reference_standards/microanalytical_RM.html), using ^{57}Fe as internal standard (Gao et al., 2013; Liu et al., 2008). GSE-1G was used as quality control to correct the time-dependent signal drift and mass discrimination. The sum concentrations of all elements, expressed as oxides according to their oxidation states in magnetite, are considered to be 100 wt.% for a given anhydrous mineral (Liu et al., 2008). Date reduction was performed by *ICPMSDataCal* (Liu et al., 2008).

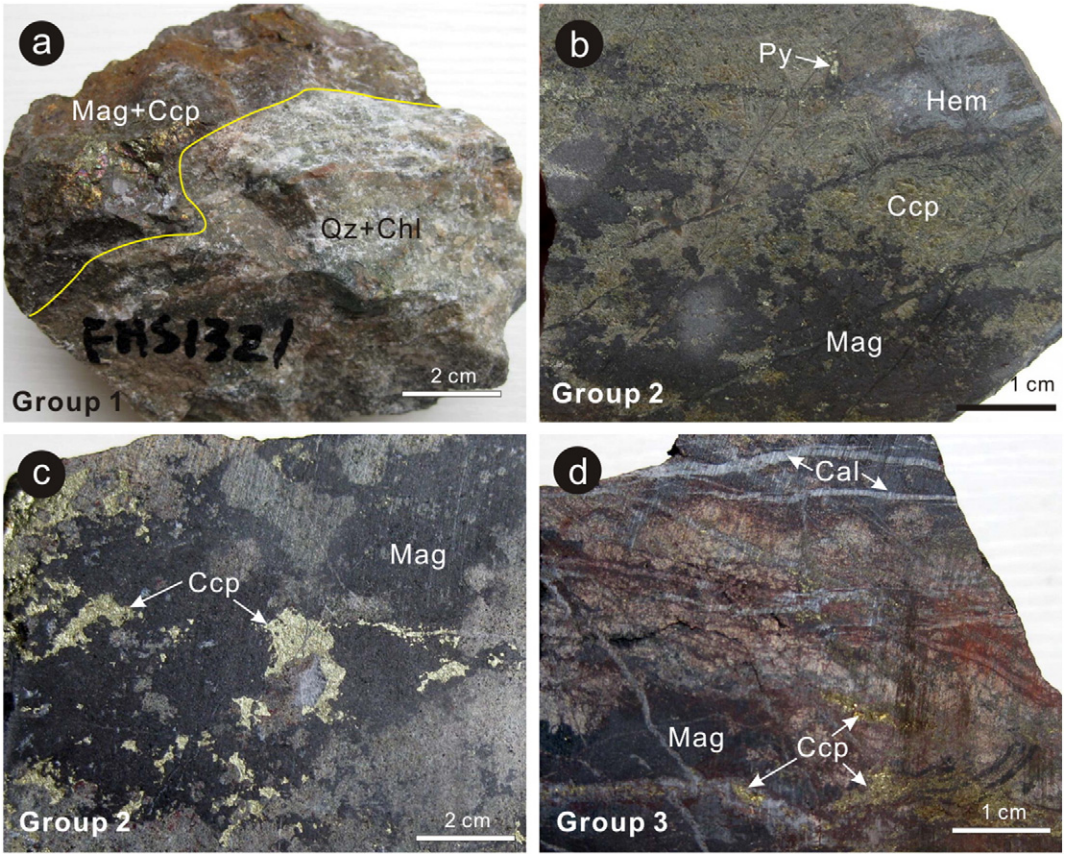

Fig. 3. Photographs of ores from different mineralization stages of the Fenghuangshan deposit. (a) Ore from the early retrograde skarn stage (Group 1) showing obvious boundary between mineralized skarn and barren skarn; (b–c) Ore from the late retrograde skarn stage (Group 2) composed of magnetite, chalcopyrite, and minor pyrite and hematite; (d) Ore from the carbonate stage consisting of magnetite, chalcopyrite and calcite. Calcite commonly occurs as veins crosscutting magnetite. Mag, magnetite; Py, pyrite; Ccp, Chalcopyrite; Hem, hematite; Cal, calcite; Qz, quartz; Chl, chlorite.

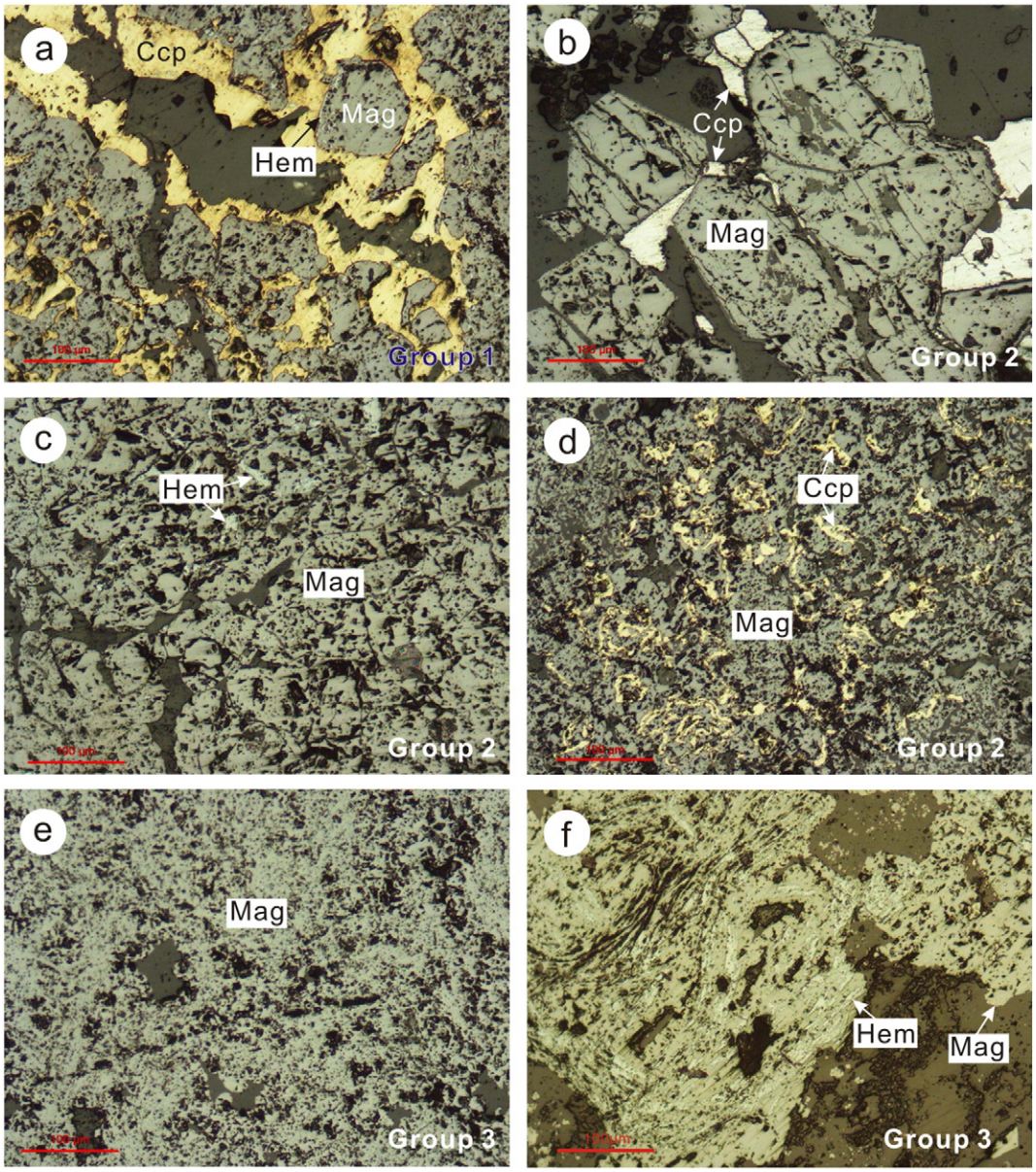

Fig. 4. Photomicrographs of ores from the Fenghuangshan deposit (under reflected light). (a) Ore from the early retrograde stage (Group 1) containing subhedral to euhedral magnetite grains which are associated with chalcopyrite and replaced by hematite along the margin; (b) Euhedral magnetite grains from the late retrograde stage (Group 2) which are 100 to 200 μm in size; (c–d) anhedral magnetite grains from the late retrograde stage (Group 2) infilled by hematite or chalcopyrite; (e–f) anhedral magnetite grains from the carbonate stage (Group 3) locally replaced by hematite. Mag, magnetite; Ccp, Chalcopyrite; Hem, hematite.

5. Analytical results

Analytical results of LA–ICP–MS for different stages of magnetite are presented in the Appendix. The average values and standard deviations of trace element contents in magnetite are listed in Table 1. The detected elements include lithophile elements, Si, Ca, Rb, Sr, Al, Ge, W, Ga, Mg, Mn, Ti, and V, and chalcophile elements, Bi, Pb, Sn, Co, and Zn. Silicon and Ca contents of magnetite range from ~3000 to ~20,000 ppm and from ~1000 to ~13,000 ppm, respectively. Magnesium and Al contents range from ~60 to 2300 ppm and from ~50 to 5000 ppm, respectively. Magnetite contains ~200 to 2000 ppm Mn, ~10 to 1000 ppm Ti, ~0.1 to 500 ppm V, Co, Zn, Ga and W, ~0.01 to <100 ppm Ge, Rb, Sr, Sn, Pb, and Bi. Some magnetite grains also have Ca, Si, Sn, and W contents lower than the detection limits (Table 1).

In general, magnetite grains from the three stages of mineralization show similar bulk continental crust normalized lithophile and chalcophile elements patterns (Fig. 6). Many elements show good correlations. Magnesium shows positive correlations with Al and Ca (Fig. 7a and b). Calcium shows a positive correlation with Si (Fig. 7c). Tin shows positive correlations with W and Pb (Fig. 7d and e). A positive correlation is also for Pb and W (Fig. 7f). There are also positive correlations of Ge versus Bi (Fig. 7g) and Ca versus Sr (Fig. 7h). However, some elements such as Co and W have different contents for different groups, varying up to four orders of magnitude (Fig. 8). For example, magnetite grains from Group 1 have the highest Co but the lowest W contents, whereas those from Group 3 contain the highest W but the lowest Co. Those from Group 2 have moderate Co and W contents (Fig. 8a). Due to different Ga and Co contents, magnetite grains from three groups define three populations (Fig. 8b). In the plot of Mn vs. Sr, magnetite grains from Group 1 overlap those from Group 2, whereas those from Group 3 have the low Mn contents different from others (Fig. 8c). Magnetite grains from Group 3 have the largest variation ranges of V and Ti

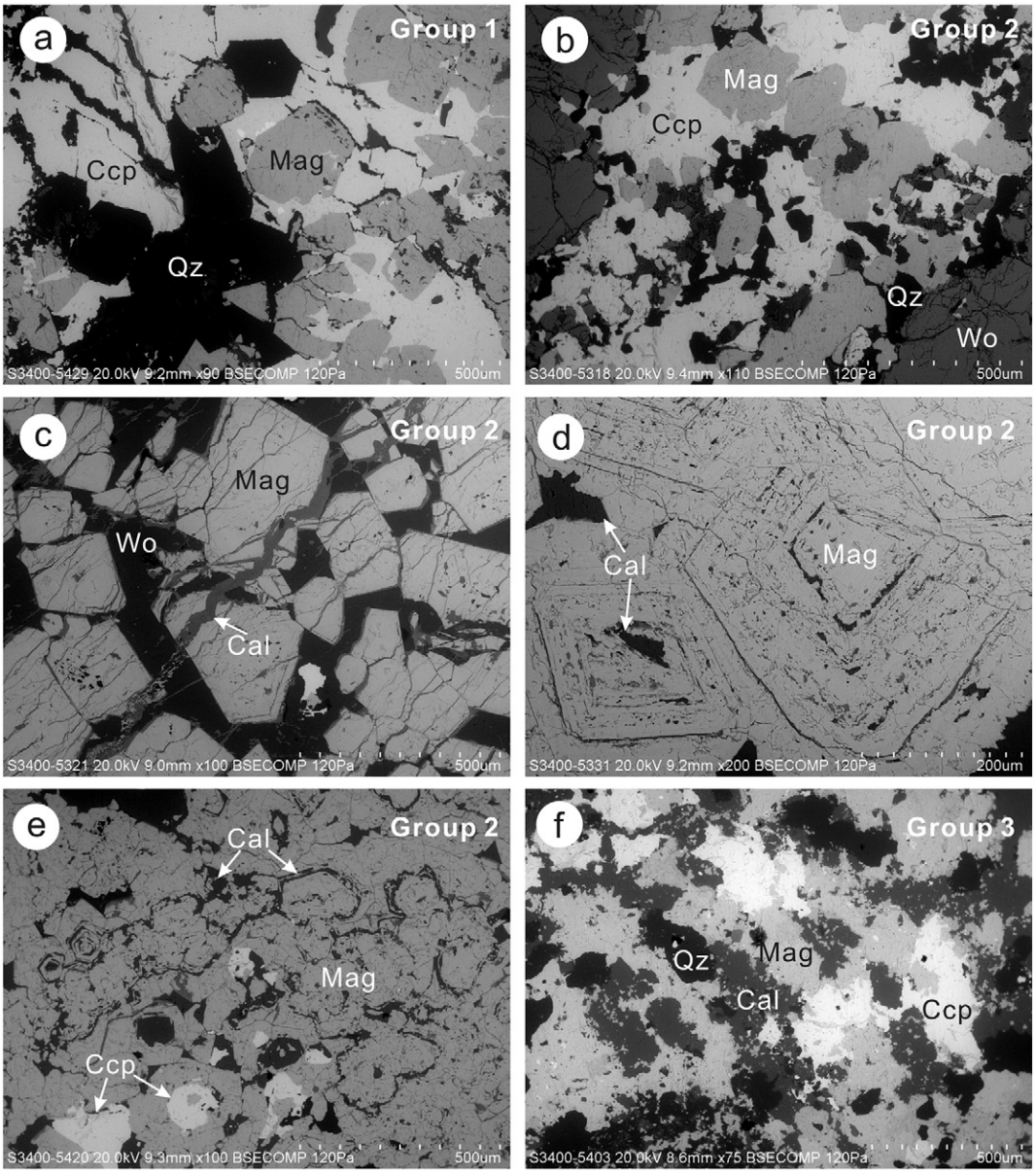

Fig. 5. BSE images of ores from the Fenghuangshan deposit. (a) Ore from early retrograde stage (Group 1) composed of magnetite, quartz, and chalcopyrite; (b) Ore from late retrograde stage (Group 2) composed of magnetite, quartz, chalcopyrite, and wollastonite; (c) Ore from the late retrograde stage (Group 2) composed of magnetite and wollastonite. The fractures of magnetite were infilled by calcite; (d–e) Magnetite grains of ore from the late retrograde stage (Group 2) replaced by calcite forming typical ringlike retrograde texture; (f) Ore from the carbonate stage composed of magnetite, chalcopyrite, quartz, and calcite. Mag, magnetite; Ccp, Chalcopyrite; Hem, hematite; Qz, quartz; Wo, wollastonite; Cal, calcite.

contents (Fig. 8d). Magnetite grains from Group 3 have higher Ti contents than those from Group 2, but both have similar V contents (Fig. 8d). Due to different Co and Ti contents, magnetite grains from different groups show distinct fields (Fig. 8e). Aluminum shows positive correlations with Ga for magnetite grains from all groups, but magnetite grains from Groups 1 and 2 define different populations relative to those from Group 3 (Fig. 8f).

In order to reveal the underlying relations among the trace element compositions of magnetite from different groups, factor analysis is performed by the statistical package SPSS Version 16 using a principal component extraction method with a Kaiser Varimax rotation (Kaiser, 1958) and a Bartlett factor score. As pointed out by Nadoll et al. (Nadoll et al., 2012), only factor scores that lie outside the −0.5 to 0.5 intervals could be meaningful for the data assessment. Rotated component matrix for the factor analysis is listed in Table 2. Selected trace elements have established three factors that account for >70% variability in the dataset (Table 2). Factors 1, 2 and 3 have element assemblages of Co–Ti–Al–Ga, Mg–Zn and V–Mn–W, respectively (Fig. 9). To describe the factor scores of individual samples for the established factors, the factor scores (only outside the −0.5 to 0.5 intervals) are plotted in the X–Y space (Fig. 10). A greater score denotes a greater significance of the respective factor for the magnetite from the corresponding deposits (Kaiser, 1958). For example, magnetite from Groups 1 and 2 has the largest scores for Factor 1 in the plots of Factor 1 versus Factor 3 and Factor 2 (Fig. 10), indicating that magnetite Groups 1 and 2 have similar Co, Ti, Al and Ga contents. Similarly, magnetite from Group 2 has the largest scores for Factor 2 (Fig. 10), indicating that Factor 2 can be used to discriminate magnetite from Group 2 from others. Magnetite from Group 3 has the large scores in the plot of Factor 3 versus Factor 1, but has similar scores with others in the plot of Factor 3 versus Factor 2 (Fig. 10). This indicates that magnetite from Group 3 has some affinity with Factor 3, but Factor 3 cannot serve as s discriminate factor.

Table 1
LA–ICP–MS results for trace elements (in ppm) in magnetite from the Fenghuangshan Cu–Fe–Au deposit, Eastern China.

Sample no.		Mg	Al	Si	Ca	Ti	V	Mn	Co	Zn	Ga	Ge	Rb	Sr	Sn	W	Pb	Bi
DL[a]		34	19	2889	715	6	1.61	8.82	0.193	7.58	0.747	1.4	0.151	0.001	1.51	0.001	0.192	0.001
FHS1306	ave (n = 12)[b]	915	1412	11502	4464	74	14.9	1315	4.95	128	97	11.3	4.06	12.4	3.91	6.70	3.57	0.80
	stdev	595	756	4462	1682	44	16.5	256	1.60	97	26	11.3	3.05	9.1	1.71	6.00	2.00	0.33
FHS1308	ave (n = 13)	757	1393	10431	3182	235	80	1310	15.4	139	24.7	28.8	3.24	17.2	2.42	7.50	4.28	5.22
	stdev	598	832	3322	1803	143	65	278	4.6	65	5.5	22.8	1.59	10.6	0.91	7.71	2.88	9.91
FHS1310	ave (n = 13)	426	854	7200	2928	28	7.76	1737	48	149	8.76	5.51	2.64	9.29	3.25	11.1	1.79	1.01
	stdev	279	872	2517	1424	27	4.55	339	4	47	3.99	4.39	1.49	7.74	1.29	8.7	0.99	1.21
FHS1313	ave (n = 11)	216	655	9920	1080	174	12.6	867	3.32	79	58.6	19.3	5.61	4.48	9.70	112	4.01	2.06
	stdev	92	279	6588	82	77	5.3	242	1.08	32	13.5	18.1	4.00	2.99	7.18	208	3.3	2.32
FHS1315	ave (n = 15)	282	467	4139	b.d.l.	64	15.6	281	1.97	132	64	9.94	3.87	6.70	11.1	94	10.6	1.92
	stdev	178	224	670		17	4.7	31	1.28	39	8	2.74	2.07	1.96	4.0	83	6.3	0.88
FHS1318	ave (n = 5)	592	2138	9175	3025	274	39.1	1320	57	100	18.8	3.48	1.89	11.9	b.d.l.	b.d.l.	2.42	0.94
	stdev	274	832	2186	1354	57	9.6	218	3	14	3.5	0.58	0.57	3.9			0.59	1.93
FHS1319	ave (n = 11)	1086	3260	9338	4867	357	13.6	903	76	144	24.6	7.92	2.09	16.1	2.43	7.41	1.53	0.14
	stdev	419	679	1202	2921	72	6.1	153	4	26	3.4	5.00	0.89	6.7	0.46	3.98	0.93	0.1
FHS1320	ave (n = 11)	742	1922	7051	2523	505	21.9	1667	62	146	23.8	5.09	1.66	7.77	b.d.l.	1.59	0.93	0.24
	stdev	381	789	2115	931	339	8.6	251	9	34	4.6	2.85	1.34	4.04		0.98	0.79	0.32
FHS1321	ave (n = 16)	895	3832	9660	3720	537	24.2	1161	127	145	27.8	4.05	3.07	12.0	b.d.l.	2.15	1.79	0.16
	stdev	209	665	2136	1385	109	6.7	175	12	39	4.9	1.95	1.66	4.0		1.85	0.65	0.13

Abbreviation: D.L. = detection limit, ave = average, stdev = standard deviation, b.d.l. = below detection limit.
[a] Detection limit (D.L.) = $3 \times \sigma^{i}_{background} \times C^{i}_{RM}/cps^{i}_{RM}$, where $\sigma^{i}_{background}$ is the standard deviation of multiple determinations of element *i* in the background, C^{i}_{RM} and cps^{i}_{RM} are concentration and peak intensity of element *i* in the reference material, respectively.
[b] Numbers in parenthesis represent the number of analyzed spots.

6. Discussion

6.1. Element behavior during the skarn formation process

Trace element pairs or groups in magnetite show different behavior in different geological environments. For example, V and Cr decrease with Ti increasing during silicate fractionation (Dare et al., 2014), whereas V and Ti would decrease with no systematic Cr variation during hydrothermal evolution (Huang et al., 2013). Magnetite from the Fenghuangshan deposit shows a positive correlation of V with Ti (Fig. 8d), characteristic of hydrothermal magnetite. Nickel and Cr also behave differently in magmatic and hydrothermal systems. In silicate magmatic processes, their behavior is coupled and Ni/Cr ratios of magnetite are commonly no more than 1, however, their behavior is decoupled in hydrothermal systems, with Ni/Cr ratios ≥1 (Dare et al., 2014).

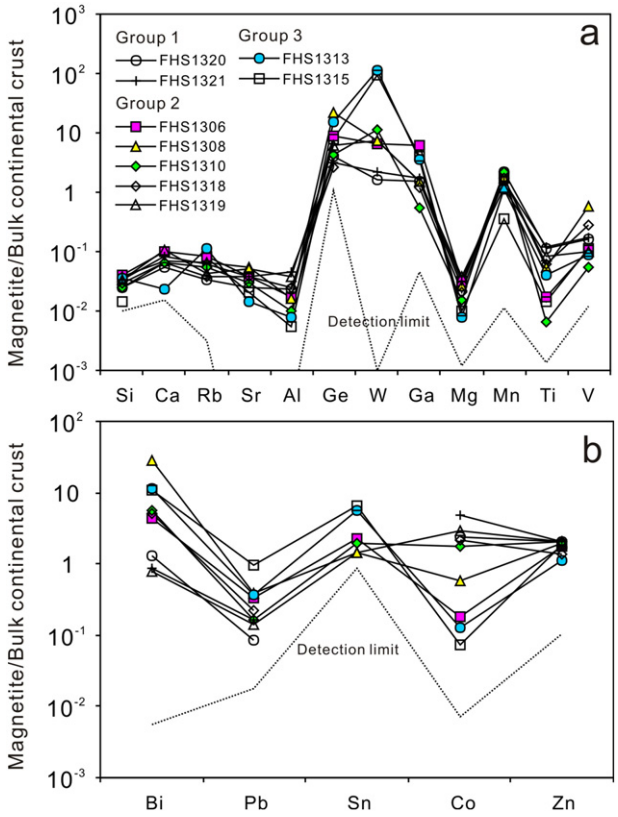

Fig. 6. Normalized multi-element variation diagrams of lithophile element (a) and chalcophile element (b) concentrations in magnetite from the Fenghuangshan deposit. Normalization values of bulk continental crust are from Rudnick and Gao (Rudnick & Gao, 2003). Elements are ordered with increase in compatibility into magnetite to the right (after Dare et al., 2012).

The behavior of elements in magnetite during the skarn formation process is not well constrained due to limited experimental data on hydrothermal magnetite. The positive correlations of Mg vs. Ca and Al, and Ca vs. Si (Fig. 7a–c) indicate that lithophile elements, Mg, Al, Ca, and Si show similar behaviors during magnetite formation in skarn systems. The good correlation of Ca and Si is also found in magnetite from the Tengtie Fe skarn deposit in the Nanling Range, South China (Zhao & Zhou, 2015). Zoned magnetite from Fe-skarn of Vegas Peledas shows similar concentration maps of Ca, Al, Mg, and Ga, also indicating their similar behaviors (Dare et al., 2014). In the Chengchao Fe skarn deposit, the primary magnetite is rich in Si, Al, and Mg, whereas the secondary variety is compositionally simple with negligible amounts of such elements (Hu et al., 2014). The contrasting compositions of the primary and secondary magnetite were interpreted as a later hydrothermal overprint that may have leached Mg, Si, Al and Ca previously locked in the early magnetite during the dissolution–reprecipitation process (Hu et al., 2014). This also indicates that Mg, Si, Al and Ca behave similarly during the skarn formation process and could have very different abundances at different stages. Therefore, the element assemblage of Mg + Al + Si + Ca in magnetite can serve as a possible discriminator in distinguishing different stages of magnetite during the skarn formation process.

Positive correlations of W versus Sn, Pb versus Sn and W versus Pb (Fig. 7d–f) indicate that these elements behave similarly during the skarn formation process. Germanium exhibits lithophile, siderophile, chalcophile, and organophile affinities in different geochemical environments (Bernstein, 1985). Germanium can partition into magnetite probably due to its siderophile nature. The strong positive correlation between Ge and Bi (Fig. 7g) indicates that Bi partitioning into magnetite is also due to its siderophile nature.

6.2. Possible factors controlling the composition of skarn magnetite

The trace element concentration of hydrothermal magnetite is controlled by various factors under different hydrothermal environments,

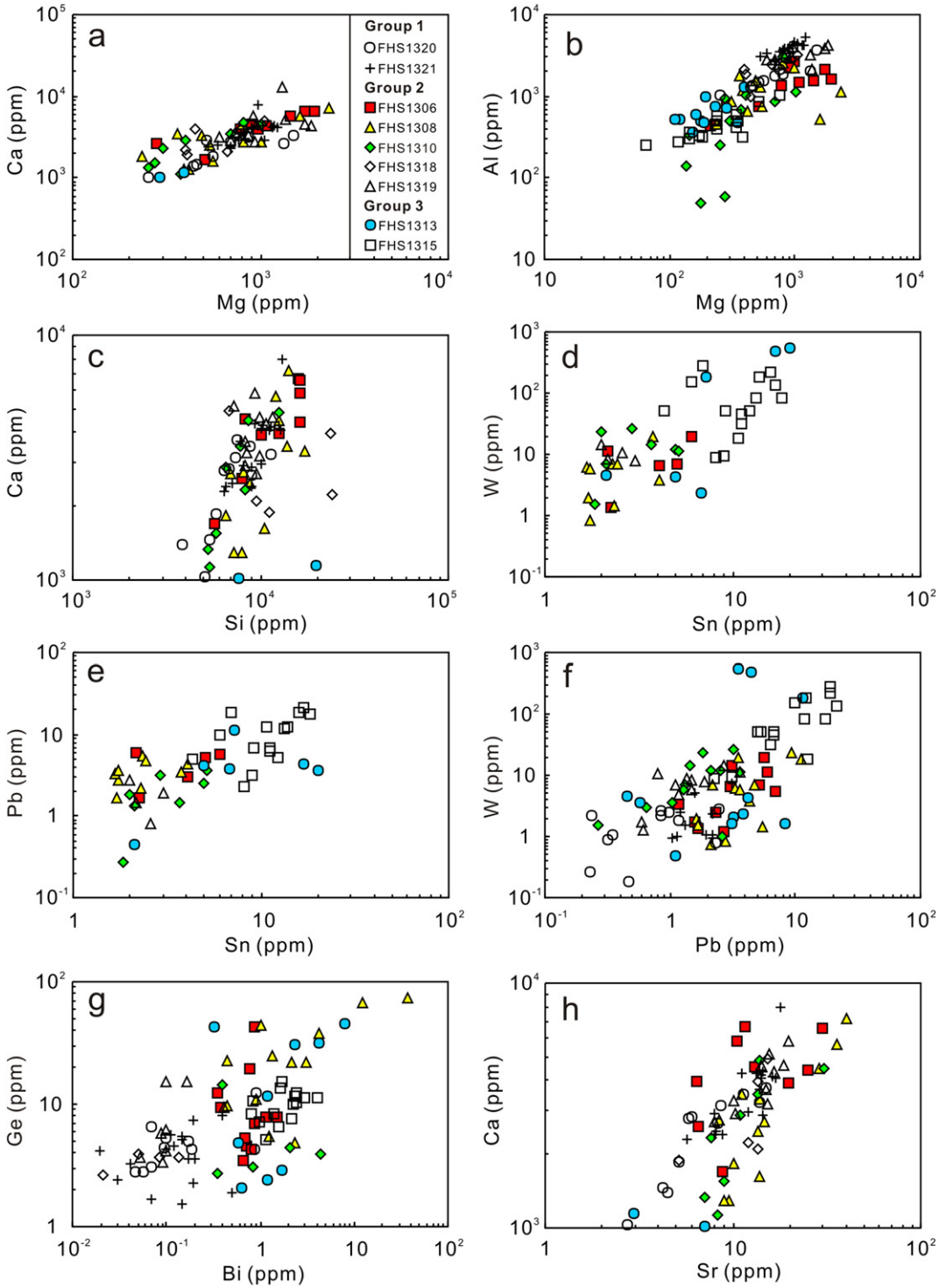

Fig. 7. Element correlation diagrams. Positive correlations of Mg vs. Ca and Al (a and b), Ca vs. Si (c), W vs. Sn (d), Pb vs. Sn and W (e and f), Ge vs. Bi (g), and Ca vs. Sr (h) are recorded.

as has been reviewed by Nadoll et al. (Nadoll et al., 2014). The concentration of an element in hydrothermal magnetite may depend on (a) the concentration of the element in the fluid from which it crystallizes, (b) fluid–rock interaction, (c) whether co-crystallizing minerals are competing for that element, and (d) physicochemical conditions such as temperature, pressure, oxygen (fO_2) and sulfur fugacity (fS_2) which affect the partition coefficient of the element into magnetite (e.g., Dare et al., 2014; Nadoll et al., 2014). The similar bulk continental crust normalized trace element patterns of magnetite in our study (Fig. 6) indicate that magnetite from Groups 1, 2 and 3 share a common source. However, magnetite from different groups also shows relative enrichment or depletion in some trace elements (Fig. 10), which would be affected by other factors. Therefore, except primary fluid composition, the other three factors will be discussed.

6.2.1. Fluid–rock interaction

In skarn systems, fluid–rock interaction or host rock buffering is considered to be the major control of trace elements in magnetite (Nadoll

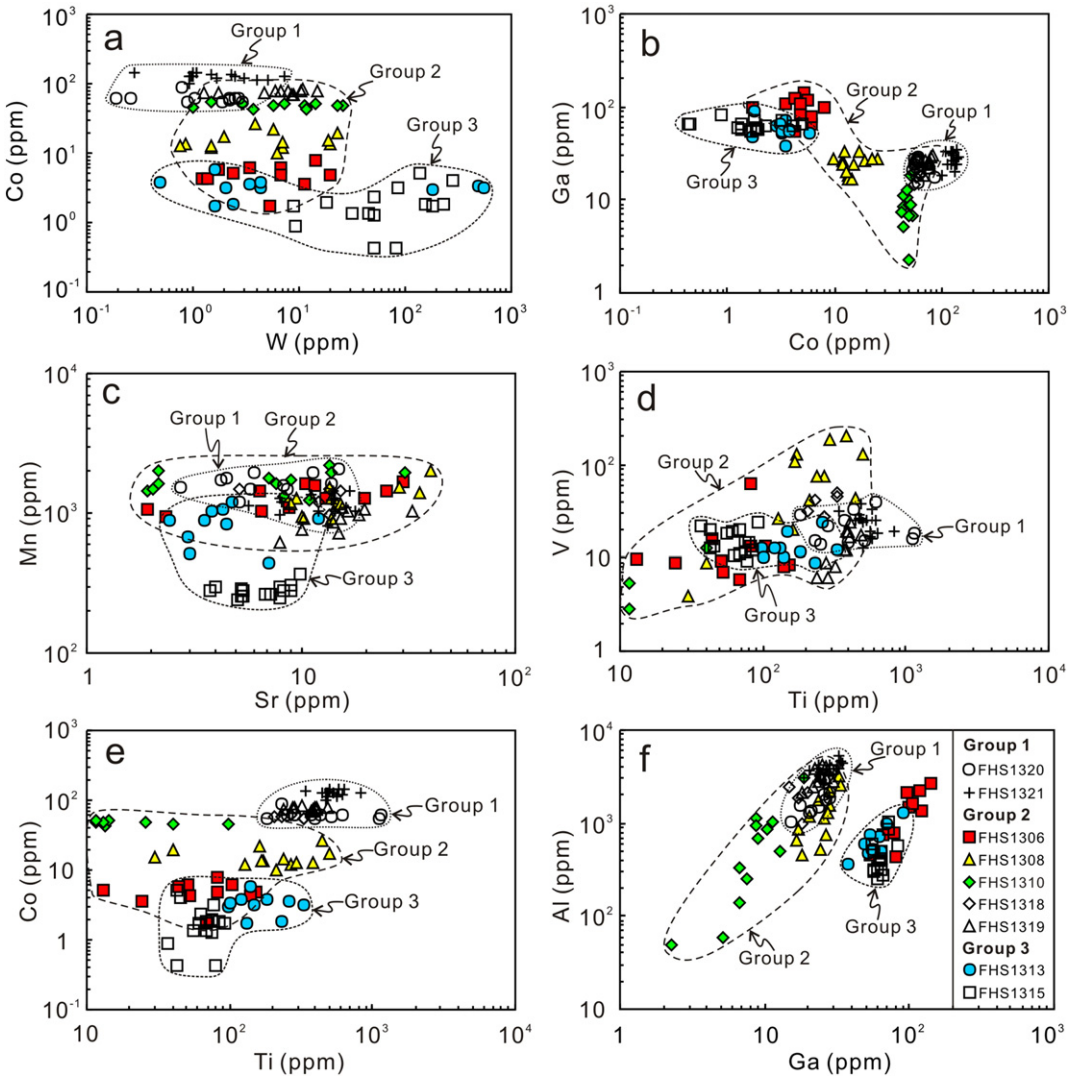

Fig. 8. Binary plot of trace element concentrations in magnetite from different groups. Groups 1 and 2 correspond to the early and late retrograde stage, respectively. Group 3 corresponds to the carbonate stage. (a) Plot of Co and W showing different compositions of magnetite from the three groups; (b) Ga vs. Co plot showing different populations for magnetite from the three groups. Cobalt concentrations decreased during the skarn formation; (c) Plot of Mn vs. Sr showing lower Mn contents in magnetite from the carbonate stage (Group 3) than those from the retrograde stages (Groups 1 and 2); (d) Plot of Ti vs. V showing similar contents of Ti and V for magnetite from the three groups; (e) Plot of Co vs. Ti showing that magnetite grains from the three stages define three separated fields due to differences in Co and Ti concentrations; (f) Plot of Al vs. Ga showing a strong positive correlation of Al with Ga for magnetite from all groups.

et al., 2014). It has been shown that elements such as Mg and Mn can successively be enriched in hydrothermal fluids by extensive fluid–rock interactions (Einaudi et al., 1981; Meinert, 1992). Magmatic fluids are generally enriched in Si, Al, Na, K, Fe, F, and Cl (Tosdal et al., 2009) and carbonate rocks are enriched in Ca, Mg, and Mn. These elements have a similar behavior during the crystallization of magnetite in skarns so that the plot of Mg + Mn and Si + Al/Mg + Mn can reflect the degree of fluid–rock interaction (Hu et al., 2014). For example, magnetite from the endoskarn of the Chenchao Fe skarn deposit in China is relatively rich in Si and Al, whereas those from the exoskarn contain relatively high Mg and Mn (Hu et al., 2014). The decreasing Si + Al/Mg + Mn values and increasing Mg + Mn contents for magnetite from endoskarn to exoskarn indicate the decreasing fluid/carbonate rock ratios (Hu et al., 2014). For the Fenghuangshan deposit, magnetite grains at the retrograde skarn stage have higher Mg + Mn and Si + Al contents than those at the carbonate stage (Fig. 11), indicating a decreasing degree of fluid–rock interaction. There is a good correlation between Al and Ga (Fig. 8f), showing their similar geochemical behaviors during the skarn formation process. Magnetite grains from Groups 1 and 2 show continuous variation of Al and Ga contents, whereas those from Group 3 define another field. This may mean a discontinuous evolution of the ore-forming fluids. The lower Ga contents in magnetite from Group 3 may also reflect the lower degree of fluid–rock interaction.

Table 2
Rotated component matrix for the factor analysis of the selected elements.

	Factor 1 (30.9%)	Factor 2 (21.5%)	Factor 3 (18.1%)
Co	0.92	0.22	0.03
Ti	0.82	0.13	0.23
Al	0.80	0.41	0.10
Ga	−0.69	0.20	−0.26
Mg	0.23	0.83	0.28
Zn	0.09	0.79	−0.02
W	−0.21	−0.08	−0.75
Mn	0.17	0.39	0.75
V	0.05	−0.44	0.56

Extraction method is principal component analysis. Rotation method is Varimax with Kaiser Normalization. Rotation converged in 5 iterations. Values in parentheses represent the variability the respective factors account for. The three established factors account for over 70% of variability in the dataset. Factor scores outside −0.5 to 0.5 are considered to be important.

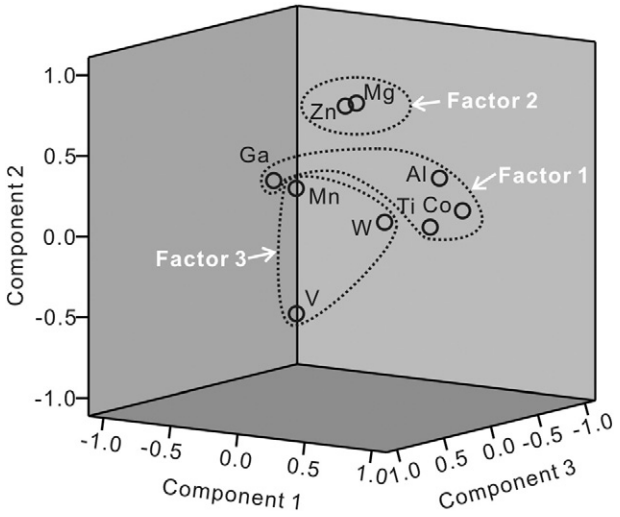

Fig. 9. Rotated component plot for the whole LA–ICP–MS dataset of magnetite from the Fenghuangshan deposit. Three factors can be indentified with different element assemblages. Factors 1, 2 and 3 have element assemblage of Co–Ti–Al–Ga, Mg–Zn, and V–Mn–W, respectively.

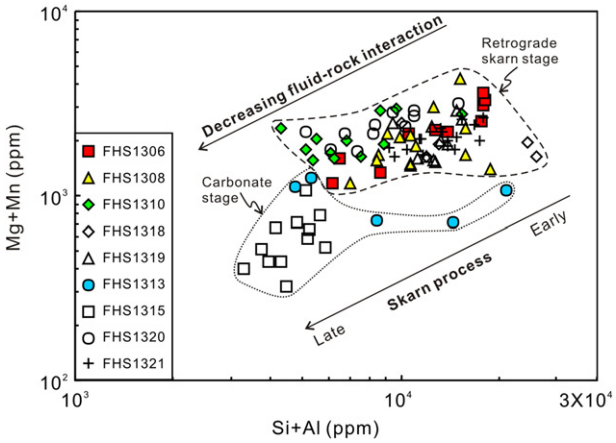

Fig. 11. Plot of Si + Al vs. Mg + Mn for LA–ICP–MS data of magnetite showing different compositions of magnetite from different stages. Magnetite grains from the retrograde stage have higher Si + Al and Mg + Mn contents than those from the carbonate stage, indicating a decreasing degree of fluid–rock interaction during the skarn formation process.

6.2.2. Precipitation of associated minerals

Minerals formed by syncrystallization with magnetite probably affect concentrations of some trace elements within the magnetite due to different partition coefficients (Dare et al., 2014; Nadoll et al., 2015). In magmatic Fe–Ti–V deposits, syncrystallizing minerals, olivine, pyroxenes, plagioclase and apatite, have little influence on trace element contents of magnetite because elements (REE, P, Li, Sc, Sr, Ba, U, Th) compatible in these silicate and phosphate minerals are incompatible in magnetite (Liu et al., 2015). On the other hand, the contents of Co, Ni, Mo, Sn, Zn and Pb in magnetite would be affected by sulfides because these elements can partition into both magnetite and sulfide phases in sulfide-bearing magmatic and hydrothermal systems. For example, in magmatic sulfide deposits, Ni partitions into magnetite and sulfides (pyrrhotite and pentlandite) when magnetite crystallizes from primitive and evolved Fe-rich monosulfide solution (MSS),

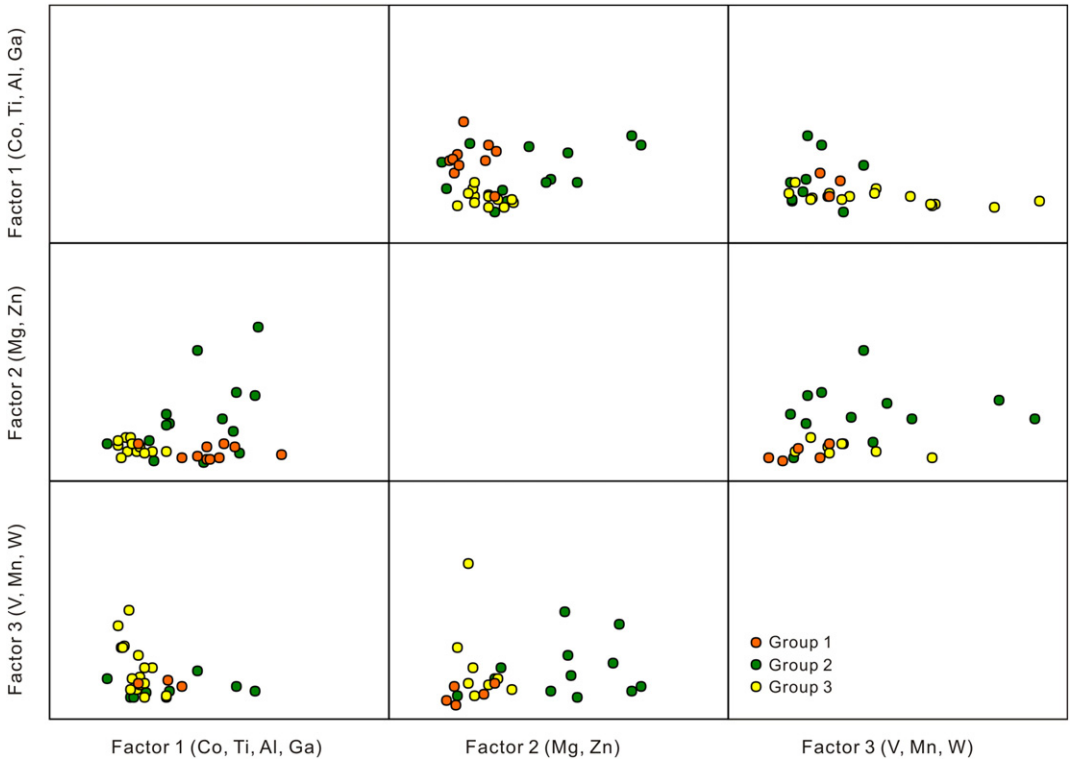

Fig. 10. Factor score scatter plots for factors 1 to 3. Only factor scores that lie outside −0.5 to 0.5 intervals are used in this plot. Magnetite from Groups 1 and 2 can be discriminated from magnetite from Group 3 due to its largest scores of factor 1 (Co–Ti–Al–Ga). Magnetite from Group 2 can be discriminated by factor 2 (Mg–Zn). Magnetite from Group 3 shows affinity with factor 3, but factor 3 cannot be served as a discriminate factor.

whereas the Ni content of magnetite increases 2- to 3-fold when magnetite crystallizes from residual Cu-rich intermediate solid solution (ISS) where pyrrhotite is absent (Dare et al., 2012). Therefore, pyrrhotite has an important effect on the Ni content of magnetite crystallized from a sulfide liquid. In contrast to Ni, the Co content of magnetite remains constant even when MSS/pyrrhotite is absent in Cu-rich ISS, indicating that Co in magnetite is not significantly affected by sulfides.

Little is known about the effect of sulfides on trace elements in magnetite from hydrothermal systems. Carew (Carew, 2004) suggested that for the Fe oxide (±Cu–Au) mineralized system in NW Queensland, Australia, both magnetite and pyrite would partition Ni in equal amounts and concluded that the presence or absence of pyrite in the same mineral assemblage may affect the amount of Ni in magnetite. However, Huang et al. (Huang et al., 2014) suggested that Co rather than Ni in magnetite was significantly affected by the associated sulfides. Chen et al. (Chen et al., 2015) proposed that coprecipitating Cu-sulfides have little effect on Co, Ni, Mo contents of magnetite from Fe–Cu deposits in the Kangdian metallogenic province of SW China.

In the diagram of Ga vs. Co (Fig. 8b), magnetite grains from different groups have plotted in different fields. Gallium increases but Co decreases in magnetite with the proceeding skarn formation process. Due to different Co contents, magnetite grains from different groups define three fields in the Co versus Ti diagram in spite of minor overlaps (Fig. 8e). From the early retrograde skarn stage, the late retrograde skarn stage, to the carbonate stage, Co decrease in magnetite. Similar trends are found in the Tengtie Fe skarn deposit in the Nanling Range of South China (Zhao & Zhou, 2015). Therefore, Co contents in magnetite would decrease during the skarn formation due to the increasing amounts of sulfides.

The positive correlation between Ca and Sr (Fig. 7h) indicates that these elements have the same geochemical affinity, which is consistent with the fact that Sr is commonly enriched in carbonate minerals such as calcite, siderite, and magnesite. Magnetite grains from Groups 1 and 2 have similar Sr and Mn contents, whereas those from Group 3 have lower Mn contents (Fig. 8c). This may indicate that Mn partitioned into carbonate minerals so that magnetite was relatively depleted in Mn at the carbonate stage.

Therefore, the presence of sulfides in the mineral assemblage would affect the content of Co in magnetite and coprecipitating carbonate would lower Mn in magnetite. However, the effect of the decreasing temperature of the fluids on the decreasing Co and Mn contents in magnetite cannot be precluded.

6.2.3. Temperature

Temperature is considered another major governing factor for the composition of hydrothermal magnetite because partition coefficients are greatly temperature dependent (McIntire, 1963). High-temperature hydrothermal porphyry and skarn magnetite shows relatively high trace element concentrations that for many elements are comparable with those in igneous magnetite, whereas unmetamorphosed magnetite from banded iron formation (BIF) has the lowest overall minor and trace element concentrations (Nadoll et al., 2014). Microthermometric studies of fluid inclusions in garnet, quartz and calcite have shown that the homogenization temperatures for the retrograde skarn stage, quartz–sulfide stage, and carbonate stage of the Fenghuangshan deposit were 448–506 °C, 222–325 °C, and 122–145 °C, respectively (Lai et al., 2007), showing a decreasing temperature during fluid evolution. There is no obvious correlation between V and Ti for magnetite from all mineralization stages (Fig. 8d). Magnetite from Group 1 has relatively high Ti contents, which can be attributed to higher formation temperatures for the early retrograde skarn stage because Ti is a good temperature indicator (Nadoll et al., 2014).

6.3. Discrimination diagrams for skarn magnetite

The trace element composition of magnetite is commonly used as an indicator for the origin of magnetite. Dupuis and Beaudoin (Dupuis & Beaudoin, 2011) proposed that the plot of Ca + Al + Mn vs. Ti + V can discriminate magnetite from IOCG, Kiruna, porphyry Cu, BIF, skarn, and Fe–Ti–V deposits. This diagram has provided good baselines for the source identification of magnetite from various ore types. Nadoll et al. (Nadoll et al., 2015) used a similar diagram to distinguish magnetite from skarn and porphyry deposits. They suggested that no discrete compositional boundaries for magnetite from those deposit types exist due to the often close genetic affiliation resulting in a large area of overlap in multielement plots. For the Fenghuangshan deposit, magnetite grains from the retrograde skarn stage plot in the skarn field and a minor number of grains from the carbonate stage plot in the undefined field due to lower Ca + Al + Mn contents (Fig. 12), confirming their hydrothermal origins. As illustrated in diagram of Ca + Al + Mn vs. Ti + V (Fig. 13a), magnetite from different types of skarn deposits plots across the boundary between skarn and other deposit types defined by Dupuis and Beaudoin (Dupuis & Beaudoin, 2011). This indicates that magnetite from skarn deposits may have more variable compositions than previously thought.

A wide variety of skarn deposits, including W, Sn, Mo, Cu, Fe, Pb–Zn, and Au deposits, can form due to differing compositions, oxidation state, and metallogenic affinities of the igneous intrusion (Meinert, 1992). Magnetite from the Fenghuangshan Cu–Fe deposit has Ca + Al + Mn and Ti + V contents similar to those from other Cu–Fe skarn (Fig. 13b), whereas magnetite from the Fe skarn deposits has similar Ti + V contents to those from the Cu, Cu–Fe, Cu–Fe–Zn and Cu–Pb–Zn skarn but displays higher Ca + Al + Mn contents (Fig. 13b). This indicates that magnetite from different types of skarn deposits may have different compositional populations.

Because Ca concentrations in magnetite are commonly below the detection limit or Ca concentrations are orders of magnitude lower than Al and Mn concentrations, Nadoll et al. (Nadoll et al., 2015) suggested removing Ca from the discriminate factor of Ca + Al + Mn. However, the carbonate host rocks of skarn deposits commonly include limestone and dolomite, which are significantly enriched in Ca and Mg and can elevate Ca and Mg in hydrothermal fluids. Magnesium concentrations are not used in the discrimination diagram, and thus the host rocks of dolomite have no significant effects on the source

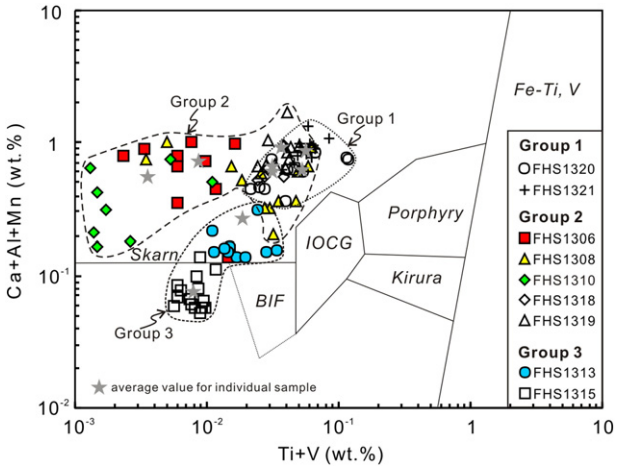

Fig. 12. Plot of Ca + Al + Mn vs. Ti + V for LA–ICP–MS data of magnetite from the Fenghuangshan deposit. Reference fields are from Dupuis and Beaudoin (Dupuis & Beaudoin, 2011). *BIF* banded iron formation, *Skarn* Fe–Cu skarn deposits, *IOCG* iron oxide-copper-gold deposits, *Porphyry* porphyry Cu deposits, *Kiruna* Kiruna apatite–magnetite deposits, *Fe–Ti, V* magmatic Fe–Ti–oxide deposits.

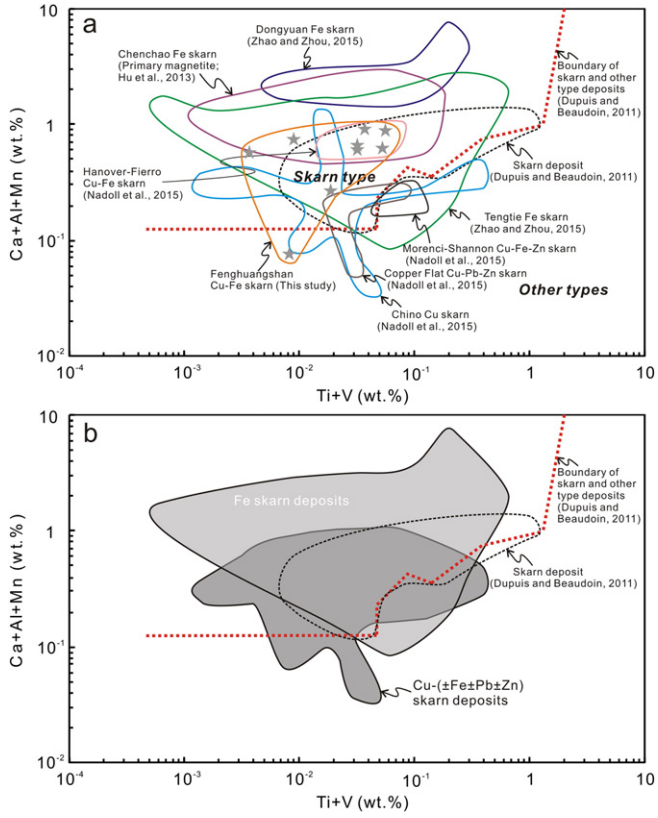

Fig. 13. (a) Plot of Ca + Al + Mn vs. Ti + V for LA–ICP–MS data of magnetite from different types of skarn deposits. Magnetite from the skarn deposits has a wider compositional range than previously thought. (b) Different trace element compositions of magnetite from Fe skarn deposits and other skarn deposits. Magnetite grains from the Fe skarn deposits have higher Ca + Al + Mn contents than those from other types of skarn deposits.

discrimination using the plot of Ca + Al + Mn vs. Ti + V. Calcium was relatively enriched in magnetite from skarn deposits. For example, zoned magnetite from skarns contains 0.1–1 wt.% Ca, which is uncommon in most other igneous and hydrothermal systems (Dare et al., 2014). Therefore, the host rock of limestone host rock has an important effect on Ca contents in magnetite and Ca in magnetite is very important for skarn systems.

7. Conclusions

Three groups of ores from different mineralization stages are identified due to different mineral assemblages and chemical compositions of magnetite. Group 1, formed at early retrograde skarn stage, is represented by disseminated magnetite, chalcopyrite, chlorite and quartz. Magnetite from Group 1 is characterized by high Co, Ti, Al and low Ga concentrations. Group 2, formed at late retrograde skarn stage, is represented by massive ore composed of magnetite and chalcopyrite with Mg and Mn enrichment in magnetite. Group 3 is formed at carbonate stage and is represented by massive ore composed of magnetite, calcite and chalcopyrite with low V, Mn and high W contents in magnetite. The positive inter-element correlations of the lithophile elements Mg, Al, Ca, and Si indicate similar behaviors for these elements during the skarn formation process. The similar behaviors are also for chalcophile elements Pb, Sn, and W during the skarn formation process. Fluid–rock interaction, precipitation of associated minerals, and temperature can control the trace element contents of magnetite from different groups. Magnetite from different types of skarns defines different compositional populations and thus there is a wider compositional range for skarn magnetite than previously thought. For skarn system, Ca is often enriched in magnetite so that it is very important and cannot be removed from the discriminate factor.

Acknowledgments

This work was jointly supported by grants from the CAS/SAFEA International Partnership Program for Creative Research Teams (Intraplate Mineralization Research Team, KZZD-EW-TZ-20), the Chinese 973 project (2012CB416804), the “CAS Hundred Talents” Project to J.F. Gao (Y5CJ038000) and the 12th Five-Year Plan Project (SKLODG-ZY125-09). Prof. Taofa Zhou from the Hefei University of Technology and the staff of the Fenghuangshan deposit helped with the field work. Dr. Patrick Nadoll, an anonymous reviewer and Prof. Franco Pirajno are thanked for their constructive comments and suggestions which have significantly improved the manuscript.

Appendix A. Full analytical results (in ppm) for Laser Ablation ICP–MS of magnetite from the Fenghuangshan Cu–Fe–Au deposit, Eastern China

Lab no.	Spot no.	Mg	Al	Si	Ca	Ti	V	Mn	Co	Zn	Ga	Ge	Rb	Sr	Sn	W	Pb	Bi
Detection limit		34	19	2889	715	6	1.61	8.82	0.193	7.58	0.747	1.4	0.151	0.001	1.51	0.001	0.192	0.001
13D14G09	FHS1306-03	510	736	5720	1708	51	9.28	1094	6.21	93	65	3.51	1.88	8.73		3.45	1.16	0.66
13D14G10	FHS1306-04	1428	1573	16282	5820	24	8.98	1640	3.49	192	106	7.75	3.45	10.5	2.14	11.1	5.91	1.51
13D14G11	FHS1306-05	977	2717	10107	3896	13	9.50	1279	5.14	106	139	4.56	3.77	19.8		2.41	2.34	0.73
13D14G12	FHS1306-06	783	1333	12556	3962	52	6.98	1456	4.32	86	122	9.32	1.42	6.41		1.21	2.70	0.38
13D14G13	FHS1306-07	904	2218	8338	4557	44	16.0	1261	5.71	58	117	5.31	4.16	13.2		1.76	1.57	0.69
13D14G14	FHS1306-08	1732	2171	15956	6629	69	5.93	1553	1.75	371	97	4.30	2.95	11.7		5.30	6.95	0.79
13D14G16	FHS1306-09	281	783	7928	2597	103	13.2	1045	5.99	107	78	19.3	11.8	6.50	4.09	6.69	3.03	0.76
13D14G17	FHS1306-10	1076	1467	16148	4433	82	13.5	1452	7.95	187	99	6.89	6.46	25.2		14.2	3.14	0.89
13D14G18	FHS1306-11	1933	1635	16241	6574	152	8.34	1672	4.83	147	106	7.76	5.24	30.0	6.04	19.7	5.65	1.17
13D14G20	FHS1306-13	214	440	5745		81	63.9	942	4.74	26	81	42.6	0.77	2.33	5.03	6.86	5.16	0.86
13D14G23	FHS1306-16	231	460			141	8.00	1071	4.34	38	54	12.5	2.75	1.93	2.25	1.39	1.65	0.36
13D14H07	FHS1308-01	554	745	10429	1613	271	76	1291	11.9	99	26.4	67.7	4.05	13.9	2.33	1.47	5.44	12.2
13D14H08	FHS1308-02	236	458	6495	1831	172	130	938	13.7	94	18.1	43.8	5.45	10.0	3.77	19.6	3.48	1.02
13D14H10	FHS1308-04	365	1786	13954	3529	128	26	1298	11.8	132	23.8	23.0	0.67	11.2	2.28	7.03	2.18	0.44
13D14H11	FHS1308-05	795	3166	12613	4506	496	131	1541	17.2	190	32.4	10.9	3.44	28.9	1.72	1.95	1.64	0.91
13D14H13	FHS1308-07	1612	533	12042	5650	30	4	1416	15.1	213	24.2		2.69	35.5		18.7	11.1	2.02
13D14H14	FHS1308-08	417	652	7908	1288	169	106	1256	13.2	82	16.8	38.1	2.47	9.43	1.74	0.85	2.81	4.21
13D14H16	FHS1308-09	1002	2215	6896	2713	446	44	1179	25.8	132	27.9	4.86	5.62	14.8	4.10	3.81	4.36	2.30
13D14H17	FHS1308-10	309	856	9853		241	76	1177	14.8	65	17.0	73.1	4.70	15.2	2.42	7.08	4.72	36.6
13D14H19	FHS1308-12	2326	1138	14084	7115	40	9	1994	19.5	302	26.0	5.47	4.23	40.3		22.7	9.22	1.27

(continued on next page)

Appendix A (*continued*)

Lab no.	Spot no.	Mg	Al	Si	Ca	Ti	V	Mn	Co	Zn	Ga	Ge	Rb	Sr	Sn	W	Pb	Bi
13D14H21	FHS1308-14	489	1571	17235	3373	213	41	918	9.86	119	27.9	25.1	3.35	14.0	1.68	6.32	3.33	1.33
13D14H22	FHS1308-15	538	1268	8716	2481	165	20	1526	22.2	169	27.3	9.82	2.88	13.6	1.73	5.80	3.56	0.45
13D14H23	FHS1308-16	810	2538	8123	2779	385	200	1317	12.5	108	33.6	22.1	1.75	8.49		1.50	1.68	3.05
13D14H24	FHS1308-17	389	1185	7258	1301	294	183	1179	13.0	109	20.3	22.0	0.76	9.03		0.75	2.10	2.15
13D14I07	FHS1310-01	1009	1104	8621	4487	40	12.8	1963	44.8	192	8.62	4.41	3.73	30.59	4.98	11.8	2.52	2.12
13D14I09	FHS1310-03	375	694	5375	1133	12	5.40	1309	49.0	167	8.86	3.05	2.71	8.31	5.14	11.3	3.64	0.82
13D14I10	FHS1310-04	276	60	4245		14		2031	43.7	231	5.20	3.90	4.90	2.14		3.65	1.05	4.49
13D14I11	FHS1310-05	179	49	5084		14		1608	50.4	154	2.27		2.84	2.15		2.89	0.64	0.63
13D14I12	FHS1310-06	136	137	5235				1437	53.2	113	6.63			1.93	1.84	1.50	0.27	0.13
13D14I13	FHS1310-07	698	846	7859	3506	13		2206	47.8	217	10.4		1.01	13.7	2.92	26.4	3.22	0.81
13D14I14	FHS1310-08	255	258	5235	1342			1755	41.6	146	7.44	2.73	0.57	7.04		11.8	2.11	0.35
13D14I18	FHS1310-11	276	939	5856	1560	12	2.88	1703	52.5	92	8.84		4.82	8.95	2.13	7.14	1.31	0.85
13D14I19	FHS1310-12	143	330	5877		26		1465	49.0	98	6.64		1.70	2.02		5.79	1.26	
13D14I20	FHS1310-13	809	3060	12442	4857	8		1948	52.1	117	18.6		2.33	13.8	3.71	14.3	1.45	0.42
13D14I21	FHS1310-14	402	1030	6531	2877	97	12.5	1232	44.4	91	11.2	14.3	4.16	10.9		0.98	2.64	0.39
13D14I22	FHS1310-15	305	489	8333	2333			1605	47.7	139	12.6		1.18	7.60	2.01	23.4	1.83	0.81
13D15D10	FHS1318-04	1044	3255	6859	4943	334	46.5	1432	55	115	24.1	3.71	2.34	15.2			1.80	0.08
13D15D14	FHS1318-08	407	1829	11202	1893	208	31.4	1487	57	89	17.2	3.93		5.19				0.05
13D15D16	FHS1318-09	399	2106		2222	234	40.7	1215	57	85	19.7	2.63		12.1				0.02
13D15D18	FHS1318-11	661	2499	9464	2105	331	49.5	985	56	114	14.8	3.67	2.08	13.6			2.97	0.13
13D15D23	FHS1318-16	448	1001		3963	266	27.2	1481	62	97	17.9		1.25	13.6			2.48	4.39
13D15E07	FHS1319-01	929	3084	9548	2708	379	12.0	611	76	182	26.4	15.5	1.67	8.03		1.25	0.61	0.17
13D15E08	FHS1319-02	1851	4276	10622	4341	490	17.2	1024	77	168	24.8	9.37	3.43	16.6	1.98	14.7	2.71	0.41
13D15E09	FHS1319-03	694	2861	8360	2940	235	6.29	907	76	146	23.7	5.73	2.94	10.4		4.71	1.17	0.09
13D15E10	FHS1319-04	729	2420	8240	3677	274	8.71	723	77	137	21.7	3.73	2.58	15.0		6.79	1.10	0.05
13D15E11	FHS1319-05	855	3396	8532	3286	403	16.4	764	73	152	24.4	6.12	1.47	10.2		1.75	0.58	0.10
13D15E12	FHS1319-06	1315	3141	9382	13173	389	19.4	1031	77	107	24.0	4.17	1.54	33.3		5.85	1.48	0.10
13D15E16	FHS1319-09	916	3780	9407	5792	285	6.05	1055	78	117	22.5		1.09	19.7	2.59	10.3	0.80	0.21
13D15E19	FHS1319-12	607	2818	9976	3230	320	8.05	902	84	170	29.9		2.27	15.3		11.0	3.63	0.12
13D15E20	FHS1319-13	1718	3921	11536	4598	401	24.0	866	78	147	28.9	15.4	1.65	14.3	3.00	7.79	1.89	0.10
13D15E22	FHS1319-15	1372	2162	7239	5154	382	19.5	1097	68	106	17.9	3.41	0.93	15.6		8.84	1.34	0.09
13D15E23	FHS1319-16	956	3997	9879	4636	370	12.4	958	71	156	26.8		3.38	18.6	2.15	8.44	1.49	0.10
13D15A07	FHS1313-01	289	705	7702	1022	97	13.0	440	2.94	166	61.6	31.6	7.74	7.05	7.25	178	11.5	4.18
13D15A08	FHS1313-02	197	1003	13417		101	10.3	514	3.46	69	70.7	30.3	6.46	3.04	16.8	480	4.40	2.32
13D15A10	FHS1313-04	353	476	4819		146	19.0	884	3.26	38	52.3	42.2	0.62	3.55	2.14	4.42	0.45	0.32
13D15A11	FHS1313-05	178	493			330	12.0	1042	3.16	62	64.5	2.91	8.90	3.86		2.02	3.19	1.68
13D15A12	FHS1313-06	235	736	3983			4.00	886	3.25	77	53.5	11.5	3.83	2.42	20.3	557	3.56	1.19
13D15A14	FHS1313-08	151	367			258	24.4	1114	3.53	67	38.0		0.61	0.70		3.48	0.58	
13D15A17	FHS1313-10	389	1313	19677	1138	232	8.92	669	1.81	84	90.1	45.7	7.38	2.99	6.76	2.39	3.81	7.82
13D15A19	FHS1313-12	186	466			139	10.0	1191	5.80	75	52.6	2.04	5.70	4.80		1.63	3.12	0.65
13D15A22	FHS1313-15	164	601			131	12.9	912	1.74	93	48.4		13.7	12.1		1.58	8.30	0.61
13D15A23	FHS1313-16	120	513			120	12.8	1059	3.78	69	57.4	4.77	0.82	4.28		0.49	1.11	0.59
13D15A24	FHS1313-17	110	531			184	11.6	827	3.79	67	55.2	2.44	5.99	4.49	4.93	4.37	4.13	1.21
13D15B07	FHS1315-01	183	313	3983		68	11.3	261	1.84	156	57	11.5	7.27	7.24	15.9	227	19.0	2.38
13D15B09	FHS1315-03	384	312	3804		42	12.9	281	5.02	129	64	10.0	7.01	9.03	16.7	137	21.5	2.21
13D15B10	FHS1315-04	241	400			63	10.7	259	2.31	131	62	7.61	2.06	5.25	4.31	52	4.95	2.13
13D15B11	FHS1315-05	173	332			83	12.1	241	1.88	123	60	6.52	2.64	5.07	6.01	152	9.89	1.60
13D15B12	FHS1315-06	337	424	4726		46	13.2	247	4.09	202	63	8.45	5.14	7.91	6.93	276	18.9	1.38
13D15B13	FHS1315-07	754	1049	4031		77	9.27	307	3.23	197	72	11.3	7.25	9.01	18.2	86	17.6	2.95
13D15B14	FHS1315-08	355	494	4721		74	11.4	299	1.97	135	56	13.5	4.36	7.99	10.6	18	12.6	1.62
13D15B16	FHS1315-09	520	843	4811		92	24.0	265	1.77	105	72	10.5	1.22	6.86	8.14	8.94	2.27	0.85
13D15B17	FHS1315-10	238	487	3227		43	19.8	282	0.44	85	65	10.4	2.72	5.38	9.21	50	6.75	2.48
13D15B18	FHS1315-11	238	566	5289		36	22.1	284	0.87	82	84	8.26	0.81	3.77	8.89	9.35	3.16	0.80
13D15B20	FHS1315-13	116	280	3034		69	20.5	289	1.34	122	66	11.1	3.30	5.28	11.1	45	6.80	4.03
13D15B21	FHS1315-14	145	298	3622		56	18.5	296	1.37	80	57	5.19	3.09	4.01	11.0	32	6.28	1.16
13D15B22	FHS1315-15	65	254	4212		75	14.6	258	1.26	98	61	7.08	2.75	5.31	12.3	51	5.26	1.00
13D15B23	FHS1315-16	343	596	4205		62	19.5	370	1.68	162	55	15.2	4.60	9.95	14.0	181	12.3	1.74
13D15B24	FHS1315-17	142	356			79	14.4	283	0.42	170	65	12.3	3.83	8.37	13.2	84	11.9	2.47
13D15F07	FHS1320-01	865	2919	7412	3147	282	22.0	1500	61	161	25.9	4.41	0.96	8.57		0.19	0.46	0.09
13D15F08	FHS1320-02	443	1265	3847	1385	255	13.8	1782	62	160	20.3			4.49		0.26	0.23	0.05
13D15F09	FHS1320-03	749	2109	8876	3537	1152	18.0	1934	61	193	27.9	3.03	1.88	11.4		2.70	0.84	0.07
13D15F11	FHS1320-05	692	1748	6446	2813	523	15.6	1478	57	202	26.8	2.83	0.64	5.80		2.20	0.23	0.05
13D15F14	FHS1320-08	255	1013	5080	1037	367	25.1	1529	60	101	15.2	2.80	0.52	2.75		2.49	0.98	0.06
13D15F16	FHS1320-09	1331	2033	8975	2696	428	32.6	1569	62	123	25.7	5.29	1.15	8.27		1.03	0.35	0.10
13D15F17	FHS1320-10	455	1342	5401	1464	182	28.5	1712	54	116	21.2	4.27	0.50	4.25		0.90	0.32	0.87
13D15F18	FHS1320-11	1508	3729	11353	3238	616	39.5	1626	61	153	29.1	12.5	2.41	13.8		2.20	0.85	0.91
13D15F19	FHS1320-12	797	1901	7558	3742	1129	15.7	2063	55	169	27.9	4.91	3.56	14.9		2.88	2.47	0.17
13D15F20	FHS1320-13	511	1515	6785	2825	390	14.3	1940	55	126	23.9	6.51	0.75	6.00		1.87	1.16	0.07
13D15F22	FHS1320-15	557	1570	5824	1869	234	15.4	1201	86	104	17.6	4.33	4.26	5.19		0.79	2.30	0.18
13D15G07	FHS1321-01	1050	4185	9000	2909	533	25.8	1275	131	158	32.8	1.89	2.34	14.4		2.47	1.19	0.50
13D15G08	FHS1321-02	767	3453	8109	2945	580	33.0	1283	141	191	24.3	8.12	2.68	8.02		1.00	1.15	0.39
13D15G09	FHS1321-03	830	3880	10116	2983	466	25.8	1039	125	100	23.9	3.30	2.76	12.0		0.94	2.18	0.04
13D15G10	FHS1321-04	693	2847	6358	2293	337	31.3	1131	134	137	24.5	1.68	0.72	5.66		1.49	1.33	0.07
13D15G11	FHS1321-05	1155	4137	11316	4231	582	16.2	1447	145	170	28.3	2.27	5.10	14.3		1.09	1.91	0.20
13D15G12	FHS1321-06	889	3830	11052	4068	636	18.6	1168	141	161	27.8	3.53	5.82	14.2		1.06	2.18	0.20
13D15G13	FHS1321-07	596	3319	7131	2472	439	24.7	1192	127	83	30.1	4.49	3.15	8.05		1.00		0.12

Appendix A (*continued*)

Lab no.	Spot no.	Mg	Al	Si	Ca	Ti	V	Mn	Co	Zn	Ga	Ge	Rb	Sr	Sn	W	Pb	Bi
13D15G14	FHS1321-08	971	4237	10355	4260	484	37.6	813	112	164	23.7	2.39	5.38	13.3		5.00	1.59	0.03
13D15G16	FHS1321-09	697	2720	8980	2394	484	26.3	957	126	91	26.1	4.19	1.66	8.00		7.22	3.11	0.02
13D15G17	FHS1321-10	1183	4184	9288	4365	619	25.5	1036	122	198	31.6	7.36	2.38	14.3		2.99		0.19
13D15G18	FHS1321-11	979	4557	13013	7978	564	19.2	1018	110	144	33.3	5.20	6.35	18.0		3.95		0.15
13D15G19	FHS1321-12	902	3781	10149	4165	571	16.9	1085	121	208	32.7	5.61	2.14	16.3		1.69		0.11
13D15G20	FHS1321-13	1233	5257	12727	4076	833	19.6	1434	125	132	32.5	3.52	2.32	16.8		0.96		0.17
13D15G21	FHS1321-14	1037	4314	12585	4291	496	13.0	1368	140	108	34.4	5.45	1.90	11.0		0.28		0.15
13D15G22	FHS1321-15	526	3015	6593	2395	472	29.4	1094	103	104	18.6	1.52	1.71	8.84		0.92	1.03	0.15
13D15G23	FHS1321-16	807	3600	7787	3690	498	24.4	1237	135	170	20.5	4.26	2.66	13.8		2.28	2.18	0.10

Notes: Blank in the data table denotes the content of the element is below detection limit.

References

Beaudoin, G., Dupuis, C., 2009. Iron-oxide trace element fingerprinting of mineral deposit types. In: Corriveau, L., Mumin, A.H. (Eds.), Exploring for iron oxide copper–gold deposits: Canada and global analogues: GAC Short Course Notes, pp. 107–121.

Bernstein, L.R., 1985. Germanium geochemistry and mineralogy. Geochim. Cosmochim. Acta 49, 2409–2422.

Carew, M.J., 2004. Controls on Cu–Au Mineralisation and Fe Oxide Metasomatism in the Eastern Fold Belt, NW Queensland, Australia (Ph.D. thesis) James Cook University, Queensland.

Chang, Y., Liu, X., Wu, Y., 1991. The Copper–iron Belt of the Lower and Middle Reaches of the Changjiang River. Geological Publishing House, Beijing (in Chinese with English abstract).

Chen, Y.-J., Chen, H.-Y., Zaw, K., Pirajno, F., Zhang, Z.-J., 2007. Geodynamic settings and tectonic model of skarn gold deposits in China: an overview. Ore Geol. Rev. 31, 139–169.

Chen, W.T., Zhou, M.-F., Gao, J.-F., Hu, R., 2015. Geochemistry of magnetite from Proterozoic Fe–Cu deposits in the Kangdian metallogenic province, SW China. Mineral. Deposita 1–15.

Dare, S.A.S., Barnes, S.J., Beaudoin, G., 2012. Variation in trace element content of magnetite crystallized from a fractionating sulfide liquid, Sudbury, Canada: Implications for provenance discrimination. Geochim. Cosmochim. Acta 88, 27–50.

Dare, S.A., Barnes, S.-J., Beaudoin, G., Méric, J., Boutroy, E., Potvin-Doucet, C., 2014. Trace elements in magnetite as petrogenetic indicators. Mineral. Deposita 49, 785–796.

Dare, S.A., Barnes, S.-J., Beaudoin, G., 2015. Did the massive magnetite "lava flows" of El Laco (Chile) form by magmatic or hydrothermal processes? New constraints from magnetite composition by LA–ICP–MS. Mineral. Deposita 50, 607–617.

Dupuis, C., Beaudoin, G., 2011. Discriminant diagrams for iron oxide trace element fingerprinting of mineral deposit types. Mineral. Deposita 46, 1–17.

Einaudi, M.T., Meinert, L.D., Newberry, R.J., 1981. Skarn deposits. Econ. Geol. 75, 317–391.

Gao, J.F., Zhou, M.F., LightFoot, P.C., Wang, C.Y., Qi, L., Sun, M., 2013. Sulfide saturation and magma emplacement in the formation of the Permian Huangshandong Ni–Cu sulfide deposit, Xinjiang, Northwestern China. Econ. Geol. 108, 1833–1848.

Hu, H., Li, J.-W., Lentz, D., Ren, Z., Zhao, X.-F., Deng, X.-D., Hall, D., 2014. Dissolution–reprecipitation process of magnetite from the Chengchao iron deposit: insights into ore genesis and implication for *in-situ* chemical analysis of magnetite. Ore Geol. Rev. 57, 393–405.

Huang, X.-W., Zhou, M.-F., Qi, L., Gao, J.-F., Wang, Y.-W., 2013. Re–Os isotopic ages of pyrite and chemical composition of magnetite from the Cihai magmatic-hydrothermal Fe deposit, NW China. Mineral. Deposita 48, 925–946.

Huang, X., Qi, L., Meng, Y., 2014. Trace element geochemistry of magnetite from the Fe(−Cu) deposits in the Hami region, Eastern Tianshan Orogenic Belt, NW China. Acta Geol. Sin. 88, 176–195 (English Edition).

Huang, X.-W., Gao, J.-F., Qi, L., Zhou, M.-F., 2015. In-situ LA–ICP–MS trace elemental analyses of magnetite and Re–Os dating of pyrite: the Tianhu hydrothermally remobilized sedimentary Fe deposit, NW China. Ore Geol. Rev. 65, 900–916.

Kaiser, H.F., 1958. The varimax criterion for analytic rotation in factor analysis. Psychometrika 23, 187–200.

Lai, J., Chi, G., 2007. CO_2-rich fluid inclusions with chalcopyrite daughter mineral from the Fenghuangshan Cu–Fe–Au deposit, China: implications for metal transport in vapor. Mineral. Deposita 42, 293–299.

Lai, J., Chi, G., Peng, S., Shao, Y., Yang, B., 2007. Fluid evolution in the formation of the Fenghuangshan Cu–Fe–Au deposit, Tongling, Anhui, China. Econ. Geol. 102, 949–970.

Li, S., Yang, X., Huang, Y., Sun, W., 2014. Petrogenesis and mineralization of the Fenghuangshan skarn Cu–Au deposit, Tongling ore cluster field, Lower Yangtze metallogenic belt. Ore Geol. Rev. 58, 148–162.

Liu, L.-M., Peng, S.-L., 2003. Prediction of hidden ore bodies by synthesis of geological, geophysical and geochemical information based on dynamic model in Fenghuangshan ore field, Tongling district, China. J. Geochem. Explor. 81, 81–98.

Liu, Y., Hu, Z., Gao, S., Günther, D., Xu, J., Gao, C., Chen, H., 2008. *In situ* analysis of major and trace elements of anhydrous minerals by LA–ICP–MS without applying an internal standard. Chem. Geol. 257, 34–43.

Liu, P.-P., Zhou, M.-F., Chen, W.T., Gao, J.-F., Huang, X.-W., 2015. In-situ LA–ICP–MS trace elemental analyses of magnetite: Fe–Ti–(V) oxide-bearing mafic–ultramafic layered intrusions of the Emeishan Large Igneous Province, SW China. Ore Geol. Rev. 65, 853–871.

Mao, J., Xie, G., Duan, C., Pirajno, F., Ishiyama, D., Chen, Y., 2011. A tectono-genetic model for porphyry–skarn–stratabound Cu–Au–Mo–Fe and magnetite–apatite deposits along the Middle–Lower Yangtze River Valley, Eastern China. Ore Geol. Rev. 43, 294–314.

McIntire, W.L., 1963. Trace element partition coefficients—a review of theory and applications to geology. Geochim. Cosmochim. Acta 27, 1209–1264.

Meinert, L.D., 1992. Skarns and skarn deposits. Geosci. Can. 19, 145–162.

Müller, B., Axelsson, M.D., Öhlander, B., 2003. Trace elements in magnetite from Kiruna, northern Sweden, as determined by LA–ICP–MS. GFF 125, 1–5.

Nadoll, P., Mauk, J.L., Hayes, T.S., Koenig, A.E., Box, S.E., 2012. Geochemistry of magnetite from hydrothermal ore deposits and host rocks of the Mesoproterozoic Belt Supergroup, United States. Econ. Geol. 107, 1275–1292.

Nadoll, P., Angerer, T., Mauk, J.L., French, D., Walshe, J., 2014. The chemistry of hydrothermal magnetite: a review. Ore Geol. Rev. 61, 1–32.

Nadoll, P., Mauk, J.L., Leveille, R.A., Koenig, A.E., 2015. Geochemistry of magnetite from porphyry Cu and skarn deposits in the southwestern United States. Mineral. Deposita 50, 493–515.

Pan, Y., Dong, P., 1999. The Lower Changjiang (Yangzi/Yangtze River) metallogenic belt, east central China: intrusion-and wall rock-hosted Cu–Fe–Au, Mo, Zn, Pb, Ag deposits. Ore Geol. Rev. 15, 177–242.

Qu, H., 2010. The Fenghuangshan copper deposit mineralization process study at Tongling, Anhui province. Chinese Academy of Geological Sciences, Beijing (in Chinese with English abstract).

Qu, H., Pei, R., Li, J., Wang, Y., 2010a. SHRIMP U-Pb dating of zircon from the Fenghuangshan quartz monzodiorite and granodiorite in Tongling Area, Anhui province and its geological implication. J. Jilin Univ. (Earth Sci. Ed.) 40, 581–590 (in Chinese with English abstract).

Qu, H., Pei, R., Wang, Y., Li, J., 2010b. Metallogenic fluid characteristic study of the Fenghuangshan Cu deposit at Tongling, Anhui province. Geosciences 24, 228–236 (in Chinese with English abstract).

Qu, H., Pei, R., Wang, Y., Li, J., 2010c. Re–Os dating of molybdenite from the Fenghuangshan skarn Cu deposit in Tongling, Anhui province and its geological significance. Acta Petrol. Sin. 26, 785–796 (in Chinese with English abstract).

Qu, H., Pei, R., Wang, H., Li, J., Wang, Y., Mei, Y., 2011. Mantle-derived ore-forming fluids of the Fenghuangshan Cu deposit, evidences form microthermometric and isotopic studies. Geol. Rev. 57, 50–62 (in Chinese with English anstract).

Qu, H., Pei, R., Fei, H., Li, J., Wang, Y., Wang, H., Yao, L., 2012. Geology, geochemistry, and geochronology of the Fenghuangshan skarn-type copper deposit in the Tongling ore cluster, Anhui Province, East China. Acta Geol. Sin. 86, 700–718 (English Edition).

Rudnick, R.L., Gao, S., 2003. Composition of the continental crust. In: Holland, H.D., Turekian, K.K. (Eds.), Treatise on geochemistry. Elsevier-Pergaman, Oxford, pp. 1–64.

Rusk, B.G., Oliver, N., Brown, A., Lilly, R., Jungmann, D., 2009. Barren magnetite breccias in the Cloncurry region, Australia; comparisons to IOCG deposits. Smart science for exploration and mining. Proceedings of the 10th Biennial Society for Geology Applied to Mineral Deposits (SGA) Meeting, pp. 656–658 (Townsville, QLD, Australia).

Shao, Y., Peng, S., Lai, J., Liu, L., Zhang, Y., Zhang, J., 2007. Identification of two types of mineralized intrusion in the Fenghuangshan copper deposit and analysis of their genesis (in Chinese with English abstract). Acta Petrol. Sin. 23, 2471–2482.

Singoyi, B., Danyushevsky, L., Davidson, G.J., Large, R., Zaw, K., 2006. Determination of trace elements in magnetites from hydrothermal deposits using the LA ICP–MS technique. CD-ROM. SEG Keystone Conference, Denver, USA.

Tosdal, R.M., Dilles, J.H., Cooke, D.R., 2009. From source to sinks in auriferous magmatic-hydrothermal porphyry and epithermal deposits. Elements 5, 289–295.

Wu, C.L., Wang, F.S., Hao, M.Y., Shi, R.D., 2000. Geochronology of intermediate-acid intrusive rocks from Tongling, Anhui. Cont. Dyn. 5, 15–23.

Zhai, Y., Yao, S., Lin, X., Zhou, X., Wan, T., Jin, F., Zhou, Z., 1992. Fe–Cu–Au metallogeny of the Middle-Lower Changjiang region (in Chinese). Geological Publishing House, Beijing.

Zhang, D., Wu, G., Di, Y., Zhang, W., Shao, Y., Yu, X., Zhang, X., Wang, Q., 2006. Emplacement dynamics of Fenghuangshan pluton (Tongling, Anhui Province): constraints from U–Pb SHRIMP dating of zircons and structural deformation. Earth Sci. J. Chin. Univ. Geosci. 31, 823–829 (in Chinese with English abstract).

Zhao, W.W., Zhou, M.-F., 2015. In-situ LA–ICP-MS trace elemental analyses of magnetite: the Mesozoic Tengtie skarn Fe deposit in the Nanling Range South China. Ore Geol. Rev. 65, 872–883.

Zhao, Y., Zhang, Y., Bi, C., 1999. Geology of gold-bearing skarn deposits in the middle and lower Yangtze River Valley and adjacent regions. Ore. Geol. Rev. 14, 227–249.